

1 **Atmospheric Response to a Collapse of the North Atlantic Circulation Under**  
2 **A Mid-Range Future Climate Scenario: A Regime Shift in Northern**  
3 **Hemisphere Dynamics**

4 Clara Orbe<sup>a,b</sup>, David Rind<sup>a</sup>, Ron L. Miller<sup>a</sup>, Larissa S. Nazarenko<sup>a,c</sup>, Anastasia Romanou<sup>a,b</sup>,  
5 Jeffrey Jonas<sup>a,c</sup>, Gary L. Russell<sup>a</sup>, Maxwell Kelley<sup>a</sup>, and Gavin A. Schmidt<sup>a</sup>

6 <sup>a</sup> *NASA Goddard Institute for Space Studies, New York, NY*

7 <sup>b</sup> *Department of Applied Physics and Applied Mathematics, Columbia University, New York, NY*

8 <sup>c</sup> *Center for Climate Systems Research, Earth Institute, Columbia University, New York, NY*

9 *Corresponding author: Clara Orbe, clara.orbe@nasa.gov*

10 ABSTRACT: Climate models project a future weakening of the Atlantic Meridional Overturning  
11 Circulation (AMOC), but the impacts of this weakening on climate remain highly uncertain. A key  
12 challenge in quantifying the impact of an AMOC decline is in isolating its influence on climate,  
13 relative to other changes associated with increased greenhouse gases. Here we isolate the climate  
14 impacts of a weakened AMOC in the broader context of a warming climate using a unique ensemble  
15 of Shared Socioeconomic Pathway (SSP) 2-4.5 integrations that was performed using the Climate  
16 Model Intercomparison Project Phase 6 (CMIP6) version of the NASA Goddard Institute for Space  
17 Studies ModelE (E2.1). In these runs internal variability alone results in a spontaneous bifurcation  
18 of the ocean flow, wherein two out of ten ensemble members exhibit an entire AMOC collapse,  
19 while the other eight recover at various stages despite identical forcing of each ensemble member  
20 and with no externally prescribed freshwater perturbation. We show that an AMOC collapse results  
21 in an abrupt northward shift and strengthening of the Northern Hemisphere (NH) Hadley Cell and  
22 intensification of the northern midlatitude jet. We then use a set of coupled atmosphere-ocean  
23 abrupt CO<sub>2</sub> experiments spanning the range 1-5xCO<sub>2</sub> to show that this response to an AMOC  
24 collapse results in a nonlinear shift in the NH circulation moving from 2xCO<sub>2</sub> to 3xCO<sub>2</sub>. Slab-  
25 ocean versions of these experiments, by comparison, do not capture this nonlinear behavior. Our  
26 results suggest that changes in ocean heat flux convergences associated with an AMOC collapse  
27 — while highly uncertain — can result in profound changes in the NH circulation and continued  
28 efforts to constrain the AMOC response to future climate change are needed.

## 29 **1. Introduction**

30 Future projections of the atmospheric circulation remain highly uncertain and reflect uncertainties  
31 in the direct radiative response to CO<sub>2</sub> forcing (Deser and Phillips (2009); Grise and Polvani (2014);  
32 Shaw and Voigt (2015); Ceppi et al. (2018)), as well as both the (direct) response to changes in  
33 sea surface temperatures (SSTs) and the (indirect) response to changes in eddy feedbacks (see  
34 Shepherd (2014) and references therein). Among the former, uncertainties in SST projections over  
35 the subpolar North Atlantic are particularly consequential, as they strongly influence the location  
36 and strength of the North Atlantic storm track, with profound downstream impacts on precipitation  
37 and wintertime weather over Europe and parts of Africa (e.g., Zhang and Delworth (2006), Smith  
38 et al. (2010), Woollings et al. (2012), O'Reilly et al. (2016)). In particular, while increases in  
39 greenhouse gases over the 21<sup>st</sup> century are expected to result in substantial warming over much of  
40 the North Atlantic, climate models project considerable cooling over midlatitudes resulting in a  
41 so-called “North Atlantic warming hole (NAWH)” (e.g., Josey et al. (2018), Drijfhout et al. (2012),  
42 Robson et al. (2016), Caesar et al. (2018)). While the drivers of this NAWH have been under  
43 considerable debate, recent detection-attribution analysis suggests that the anthropogenic signal  
44 of the NAWH has emerged from internal climate variability and, moreover, that this cooling can  
45 be attributed to declining northward oceanic heat flux over recent decades related to increased  
46 greenhouse gas emissions (Chemke et al. (2022)).

47 Among other mechanisms contributing to the development of the NAWH, the slowdown of  
48 the Atlantic Meridional Overturning Circulation (AMOC) has been invoked as one potential key  
49 driver (Cheng et al. (2013), Rahmstorf et al. (2015), Menary and Wood (2018)). Studies have  
50 long shown that changes in the strength of the AMOC can have widespread impacts not only  
51 on other components of the ocean circulation but, more generally, on the broader atmospheric  
52 climate system, resulting in a southward shift of the intertropical convergence zone (ITCZ) (e.g.,  
53 Zhang and Delworth (2005), Vellinga and Wood (2008), Jackson et al. (2015)), a strengthening  
54 of the Walker circulation (e.g., Vial et al. (2018), Orihuela-Pinto et al. (2022)) and a northward  
55 shift of the Northern Hemisphere (NH) jet stream (e.g., Liu et al. (2020), Bellomo et al. (2021)).  
56 Understanding the global scale atmospheric response to changes in AMOC strength is important  
57 not only for projections of future climate, but also for understanding paleoclimate records and  
58 the dynamics of past Dansgaard-Oeschger events. In particular, while the future collapse of an

59 AMOC is still considered unlikely, the latest generation of coupled climate models project stronger  
60 weakening with future warming, compared to older generations of models (Weijer et al. (2020)).

61 In addition to its impacts on global precipitation, SST-related changes in the AMOC can change  
62 the baroclinicity of the atmosphere, which can result in changes in the storm tracks (Woollings  
63 et al. (2012)). However, the precise impacts of a weakened AMOC on atmospheric baroclinity  
64 are not well understood, largely because studies have used models that exhibit a wide diversity  
65 in the amplitude and spatial extent of the NAWH (Gervais et al. (2019), Haarsma et al. (2015),  
66 Menary and Wood (2018)). Nonetheless, despite these uncertainties in the drivers and extent of  
67 the NAWH, Woollings et al. (2012) showed that the response of the North Atlantic storm track to  
68 climate change was singularly shaped by changes in ocean-atmosphere coupling.

69 The role of the AMOC in future projections of the jet stream in the Climate Model Intercom-  
70 parison Project Phase 5 (CMIP5) and Phase 6 (CMIP6) models was recently examined in Bellomo  
71 et al. (2021) (hereafter KB2021), who showed that changes in the AMOC play a primary role  
72 in determining the magnitude of the projected poleward displacement of the NH zonal mean jet  
73 stream. In particular, by stratifying models according to the strength of their projected AMOC  
74 weakening (in response to a quadrupling of CO<sub>2</sub>), the authors showed that models with a larger  
75 AMOC decline (> 7 Sv, relative to preindustrial values) exhibit minimum warming over the North  
76 Atlantic, a southward displacement of the ITCZ and a poleward shift of the northern midlatitude  
77 jet. The results from KB2021 suggest that the AMOC is a major driver of intermodal uncertainty  
78 in future projections of the northern jet stream (and associated hydrological impacts).

79 A key challenge in quantifying the impact of AMOC uncertainties on future projections of the  
80 large-scale atmospheric circulation is in isolating its influence on climate, relative to other changes  
81 associated with increased greenhouse gases. Thus, while the results from KB2021 are compelling,  
82 that study drew conclusions based on the spread among models subject to the same abrupt 4xCO<sub>2</sub>  
83 forcing and it is not clear if the models exhibiting greater AMOC weakening were also models  
84 that exhibit other characteristics that would independently impact the jet stream. At the same time,  
85 previous studies using more traditional freshwater flux perturbations to examine the jet (and other  
86 climate) responses to a weakened AMOC, have done so in the absence of other background changes  
87 related to increased CO<sub>2</sub> (e.g., Zhang and Delworth (2005), Jackson et al. (2015)). As such, these



88 studies may produce a circulation response to a weakened AMOC that is different than what might  
89 occur if other factors impacting atmospheric temperature gradients are included.

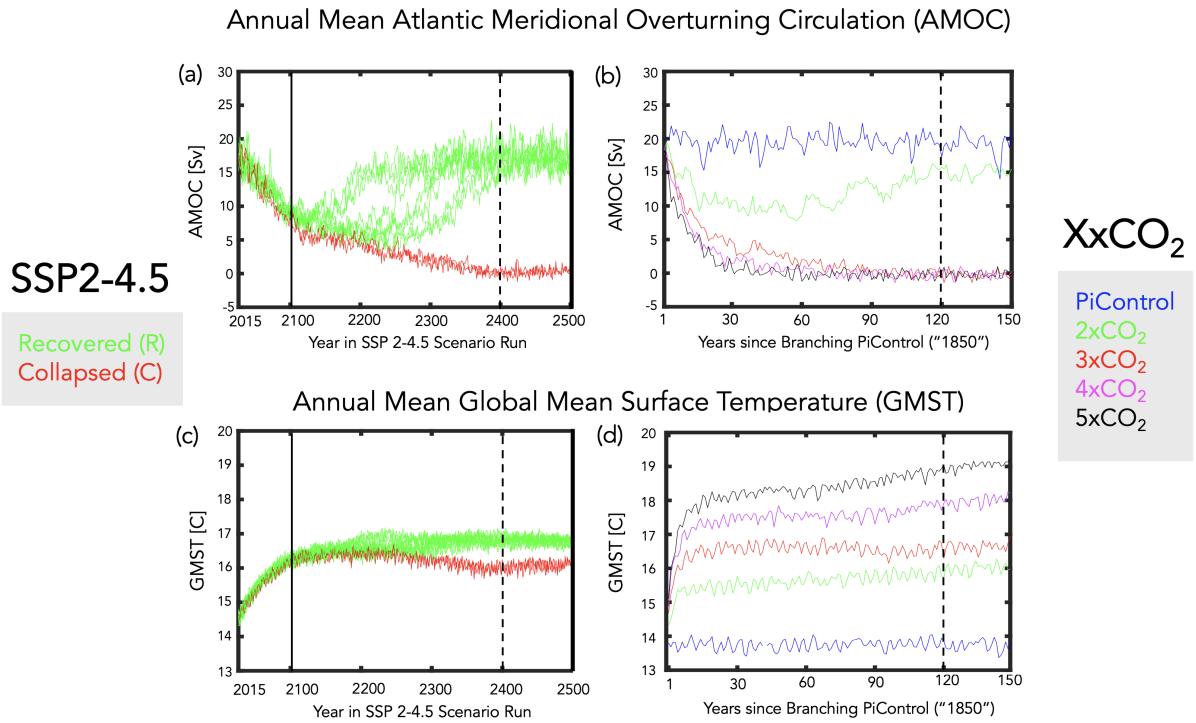
90 One recent attempt to isolate the climate impacts of a weakened AMOC in the broader context  
91 of a warming climate was performed in Liu et al. (2020). In that study, the authors compared fully  
92 coupled Representative Concentration Pathway (RCP) 8.5 simulations (Riahi et al. (2011)) using a  
93 full physics comprehensive model (CCSM4) with identically forced simulations in which a negative  
94 freshwater perturbation over the subpolar North Atlantic was added after year 1980 in order to  
95 maintain the AMOC strength (while preserving all other forcings). That study showed results  
96 that were generally consistent with KB2021, pointing to a major role of the AMOC in causing  
97 widespread cooling stretching from NH high latitudes to the tropics and a poleward displacement  
98 of the NH midlatitude jet.

99 While the results from Liu et al. (2020) represent an important step forward in isolating the  
100 impacts of the AMOC on the storm tracks in the context of a warming climate, it is not clear  
101 that prescribing a negative freshwater perturbation does not potentially interfere with nonlinear  
102 components of the AMOC response in a coupled system. To this end, here we present new results  
103 featuring an ensemble of Shared Socioeconomic Pathway (SSP) 2-4.5 integrations (Meinshausen  
104 et al. (2020)) that was performed using the CMIP6 version of the NASA Goddard Institute for  
105 Space Studies (GISS) ModelE (E2.1) (Kelley et al. (2020)). In particular, we show results from a  
106 subset of the runs documented in Romanou et al. (Under Review) (hereafter AR2023), in which  
107 the authors identified a tipping point in the SSP 2-4.5 ensemble occurring during the “extended”  
108 portion of the simulations (i.e. beyond year 2090, after which CO<sub>2</sub> emissions are ramped down).  
109 During this time period the authors show that internal variability alone results in a spontaneous  
110 bifurcation of the ocean flow, wherein two out of ten ensemble members exhibit an entire AMOC  
111 collapse, while the other eight recover at various stages (Figure 1a). Note that, in contrast to  
112 the aforementioned freshwater hosing studies, in which an AMOC collapse is induced by adding  
113 freshwater, in these experiments the AMOC collapse is caused by a reduction in evaporation from  
114 the ocean, mediated by sea ice melting (AR2023). As such, the atmospheric configuration that is  
115 used to produce this effect in an interactive mode is likely to be very different from an atmosphere  
116 which is simply responding to a prescribed freshwater flux perturbation.

117 Whereas AR2023 focused primarily on the oceanic conditions giving rise to this divergence in  
118 AMOC behavior among different ensemble members, here we focus on the subsequent impacts  
119 this has on the atmospheric large-scale circulation. In particular, we contrast the behavior between  
120 two and eight ensemble members in which the AMOC respectively collapses and recovers to  
121 historical values by year 2400 (red vs. green lines, Fig. 1a). As such, we isolate the impact of  
122 a weakened AMOC on the atmospheric circulation in the presence of increased greenhouse gas  
123 warming using a single model (unlike KB2021) and without any need to invoke negative freshwater  
124 perturbations (as in Liu et al. (2020)). To the best of our knowledge, this represents the first time  
125 that the AMOC imprint on the circulation has been isolated in the context of background increases  
126 in greenhouse gases using a fully coupled comprehensive model, absent any externally imposed  
127 freshwater perturbations that may potentially interfere with the model's internal dynamics.

128 As discussed in AR2023, the ensemble members in which the AMOC collapses are substantially  
129 cooler than those runs in which it recovers, with wintertime global mean surface temperature  
130 (GMST) differences of about 1°C by year 2400 (Fig. 1c). Therefore, in documenting the influence  
131 of the AMOC on the atmosphere in the different SSP 2-4.5 ensemble members it is natural to  
132 ask how the large-scale thermodynamic and dynamical circulations scale with these differences  
133 in GMST. Though perhaps naive, it is common practice to assume that the climate system scales  
134 linearly with GMST, as reflected in the use of so-called “global warming levels” in the recent  
135 IPCC AR6 report (James et al. (2017)) and the widely applied related practice of “pattern scaling”  
136 (e.g., Santer et al. (1990), Tebaldi and Arblaster (2014)). Recent studies, however, have shown that  
137 the climate's so-called “dynamical sensitivity” – in particular, circulation shifts associated with  
138 changes in the Hadley Cell and storm tracks - do not scale with equilibrium climate sensitivity  
139 (Grise and Polvani (2016), Ceppi et al. (2018)). As those studies, however, focused on large  
140 (CMIP5) multi-model ensembles, it is not clear if similar conclusions also apply to single models  
141 and to climate states in which the AMOC has undergone a substantial weakening. More precisely,  
142 it remains unclear how much of the circulation response to a weakened AMOC is related simply  
143 to changes in GMST or, rather, to changes in (free-tropospheric) meridional temperature gradients  
144 away from the surface.

145 To this end, in addition to reporting on the results from the SSP 2-4.5 ensemble we also examine a  
146 suite of abrupt 1-5xCO<sub>2</sub> experiments that were conducted using the same model version (Mitevski



156 FIG. 1. Top: Evolution of the annual mean maximum overturning stream function in the Atlantic ocean,  
 157 evaluated at 48°N, compared among the SSP 2-4.5 (8) recovered and (2) collapsed ensemble members (top, left)  
 158 and among the abrupt XxCO<sub>2</sub> runs (top, right). Bottom: Same as top panels, except showing annual mean global  
 159 surface temperature (GMST). Vertical solid lines mark the beginning of the “extension” portion of the SSP 2-4.5  
 160 scenario. Vertical dashed lines indicate the years after which climatological averages are evaluated (i.e., years  
 161 2400-2500 (left) and years 120-150 (right)).

147 et al. (2021)). In particular, we exploit the fact that between 2xCO<sub>2</sub> and 3xCO<sub>2</sub> abrupt forcing  
 148 the AMOC respectively recovers and collapses by year 150 (Fig. 1b), behavior which is generally  
 149 similar to the differences in AMOC responses between the recovered and collapsed members of  
 150 the SSP 2-4.5 ensemble, hereafter referred to as SSP 2-4.5 R and SSP 2-4.5 C, respectively (Fig.  
 151 1a). However, by spanning a much broader range of GMST responses, compared to the SSP 2-4.5  
 152 ensemble – and assuming that the atmospheric responses to an AMOC collapse are similar between  
 153 the 3xCO<sub>2</sub> and SSP 2-4.5 collapsed ensemble members (a point which we examine in Section 3a3)  
 154 – the broader set of XxCO<sub>2</sub> experiments affords a unique opportunity to investigate the relationship  
 155 between dynamical and equilibrium climate sensitivity in the presence of a collapsed AMOC.

162 In Section 3 we begin by contrasting the large-scale atmospheric circulation responses between  
163 the SSP 2-4.5 R and C members in which the AMOC recovers and remains collapsed after year  
164 2400 (Sections 3a1-2, Q1 below). We then compare this behavior with the circulation differences  
165 occurring in the 2xCO<sub>2</sub> and 3xCO<sub>2</sub> integrations (Section 3a3, Q2). After showing that the 3xCO<sub>2</sub>  
166 circulation changes in the NH are largely dominated by the behavior of the AMOC, we then use the  
167 broader set of 1-5xCO<sub>2</sub> abrupt experiments to examine how the collapse of the AMOC modulates  
168 the relationship between the NH dynamical circulation and GMST over a much broader range of  
169 CO<sub>2</sub> forcing (Section 3b, Q3). In addressing the latter we also use slab-ocean model integrations  
170 in order to examine if the behavior exhibited in the coupled atmosphere-ocean runs is reflected in  
171 simulations in which ocean heat flux convergence changes associated with an AMOC collapse are  
172 not allowed to occur.

173  
174 The main goals of the manuscript are centered around addressing these three questions:

175  
176 Q1) How does a collapse of the AMOC influence the atmospheric circulation in the pres-  
177 ence of the same background CO<sub>2</sub> forcing (SSP 2-4.5 ensemble)?

178  
179 Q2) How does this compare with the response to an AMOC collapse induced by different  
180 CO<sub>2</sub> forcing (2xCO<sub>2</sub> vs. 3xCO<sub>2</sub>)?

181  
182 Q3) Are AMOC-related circulation changes mediated primarily by GMST or by changes  
183 in atmospheric temperature gradients?

184  
185 In addressing Q1-Q3 we show that the AMOC tipping point described in AR2023 results in a  
186 vastly different atmospheric response between ensemble members in which the AMOC collapses  
187 versus members in which the AMOC recovers. In particular, in our model the atmospheric response  
188 to an AMOC collapse (occurring on the timescales addressed in this study) reflects a regime shift  
189 between a climate state in which the NH Hadley Cell and midlatitude jet are substantially weaker and  
190 displaced further equatorward (strong AMOC) compared to a state in which they are substantially  
191 stronger and displaced poleward (weak AMOC).

## 192 2. Analysis/Methods

### 193 *a. Models and Experiments*

194 Here we use simulations from two sets of experiments produced using the GISS version E2.1  
195 climate model (GISS-E2-1-G) (Kelley et al. (2020)), which consists of a 40-level atmospheric model  
196 with a horizontal resolution of  $2^\circ \times 2.5^\circ$  latitude/longitude coupled to the  $1^\circ$  horizontal resolution  
197 40-level GISS Ocean v1 (GO1) model (for more details of GO1 see AR2023). Comprehensive  
198 reviews of this model’s response to historical and future climate change simulations are provided  
199 in Miller et al. (2021) and Nazarenko et al. (2022), respectively.

200 We first examine results from the SSP 2-4.5 ensemble that contributed to the official submission of  
201 the NASA-GISS climate group to CMIP6. In particular, we contrast the behaviors of eight members  
202 in which the AMOC has recovered by year 2400 (SSP 2-4.5 R) with two members in which it has  
203 remained collapsed (SSP 2-4.5 C) (Fig. 1a). As discussed in AR2023, this contrasting behavior  
204 emerges during the “extension” portion following year 2090, beyond which  $\text{CO}_2$  concentrations  
205 slow down in growth from 597 ppm to 643 ppm at year 2200 and decline thereafter (Meinshausen  
206 et al. (2020)). That study further showed that the divergence in the behavior of the AMOC results  
207 from stochastic variability associated with sea-ice transport and melting in the Irminger Sea that  
208 led to a reduction in evaporation and salinity. Note that, whereas AR2023 was primarily focused  
209 on identifying the mechanisms leading to different recovery times among the SSP 2-4.5 R, our  
210 interest is in quantifying the impact of an AMOC collapse on the large-scale circulation after year  
211 2400 up to year 2500. To this end, we treat the SSP 2-4.5 R and C simulations as comprising two  
212 distinct “recovered” and “collapsed” ensembles.

213 To put the SSP 2-4.5 results in a broader context, we also examine the coupled atmosphere-ocean  
214 1-5x $\text{CO}_2$  abrupt  $\text{CO}_2$  experiments reported in Mitevski et al. (2021), which were performed using  
215 the same version of the model. We restrict our attention to a subset of the runs, focusing mainly  
216 on the 2x $\text{CO}_2$  and 3x $\text{CO}_2$  runs, but also including results from the 4x $\text{CO}_2$  and 5x $\text{CO}_2$  simulations  
217 when commenting on the linearity of the atmospheric circulation responses with respect to changes  
218 in GMST (Section 3b). As shown in Figure 1, the behavior of the AMOC by the end of the abrupt  
219 2x $\text{CO}_2$  and 3x $\text{CO}_2$  runs is generally very similar to the AMOC behavior in the SSP 2-4.5 R  
220 and C ensemble members, respectively, past year 2400. This similar behavior also appears at

221 lower latitudes ( $26^{\circ}\text{N}$ ) (not shown), consistent with the findings in AR2023, who showed a strong  
222 correlation in AMOC strength at these two latitudes (0.97) within the broader SSP 2-4.5 ensemble.

223 In addition to the results from the fully coupled ocean-atmosphere model (hereafter FOM) SSP  
224 2-4.5 and  $Xx\text{CO}_2$  integrations, we also show results from q-flux or slab-ocean model (SOM)  
225 integrations spanning the range 1- $5x\text{CO}_2$ . In these experiments any changes in ocean horizontal  
226 heat transport and vertical heat uptake by the deep ocean are not included as the ocean heat flux  
227 convergences in the mixed layer ( $-\nabla \cdot (vT)$ , including both horizontal and vertical heat fluxes) are  
228 calculated using preindustrial control values. At the same time, the SOM experiments do capture  
229 the mixed layer temperature changes resulting from changes in the net surface heat fluxes (hereafter  
230 referred to as “thermodynamic” ocean coupling). As such, contrasting the responses in the FOM  
231 and SOM experiments isolates the role of dynamic (i.e. ocean heat flux convergence) coupling on  
232 the atmospheric responses in the FOM simulations, consistent with the presentation in Chemke et al.  
233 (2022). Note that this approach does not explicitly isolate the contribution of changes in SSTs to the  
234 atmospheric circulation response, as the SST response reflects both changes in thermodynamic and  
235 dynamic ocean-atmosphere coupling. However, robustly isolating the impact of SSTs can be tricky  
236 as previous studies utilizing prescribed SST “warming hole” patterns have shown large sensitivity  
237 to how these patterns are prescribed, particularly in relation to SST gradients (see discussion in  
238 Gervais et al. (2019)).

### 239 *b. Temporal Averaging and Spatial Domains*

240 To compare the atmospheric responses from the SSP 2-4.5 simulations with those from the abrupt  
241  $\text{CO}_2$  experiments we focus on climatological averaging periods during which the characteristics  
242 of the AMOC are similar, i.e., years when the AMOC has recovered in the  $2x\text{CO}_2$  and SSP 2-4.5  
243 R runs, while the AMOC has remained collapsed in the  $3x\text{CO}_2$  and SSP 2-4.5 C experiments.  
244 As indicated in Figure 1 (dashed black vertical lines) this corresponds to years beyond which the  
245 maximum value of the overturning stream function at  $48^{\circ}\text{N}$  has reached nearly zero, corresponding  
246 to years 120-150 and 2400-2500 in the  $Xx\text{CO}_2$  and SSP 2-4.5 integrations, respectively. We refer  
247 to these periods hereafter as the “equilibrated” responses in the model, bearing in mind that the  
248 AMOC exhibits multi-centennial instability as was illustrated in an older version of the GISS

249 climate model (Rind et al. (2018)). Variations on these longer timescales are not addressed in this  
250 study.

251 We begin by presenting differences in climatological means between the SSP 2-4.5 R and C  
252 ensembles and between the 2xCO<sub>2</sub> and 3xCO<sub>2</sub> integrations. Statistical significance of the SSP  
253 2-4.5 C-R differences is assessed using a Welch’s t-test, given the unequal sample sizes represented  
254 by the 8-member R and two-member C ensembles. A two-sample Student’s t-test is used when  
255 comparing the abrupt CO<sub>2</sub> responses. In addition, when putting the SSP 2-4.5 results in the context  
256 of the broader 1-to-5xCO<sub>2</sub> forcing range we define all responses relative to a 150-year average over  
257 the preindustrial control simulation from which the abrupt CO<sub>2</sub> experiments are “branched.”

258 For the majority of the analysis considered here we focus on December-January-February (DJF)  
259 and over the NH. Our focus on DJF is consistent with the presentation in AR2023, while our  
260 focus on the NH is motivated by Mitevski et al. (2021), who showed that the AMOC collapse  
261 occurring between 2xCO<sub>2</sub> and 3xCO<sub>2</sub> results in a non-monotonic response in global mean surface  
262 temperature, driven primarily by changes occurring in the NH (more precisely, the North Atlantic).  
263 We deviate from this convention, however, at two different points in this study. First we use annual  
264 mean GMST when evaluating the dynamical sensitivity scaling in Section 3b; second, we present  
265 the energy budget analysis in Section 3c using annual means in order to facilitate comparison with  
266 previous studies. Some results about the Southern Hemisphere (SH) circulation response are also  
267 presented, but only discussed briefly.

268 Finally, while our main focus is on the “equilibrated” responses defined above, we are also  
269 interested in exploiting the evolution of the responses, as in Grise and Polvani (2017) and Chemke  
270 and Polvani (2019). As shown in those studies, consideration of the response timescales of different  
271 variables affords insight into possible mechanisms governing their evolution.

### 272 *c. Scaling with Global Mean Surface Temperature (GMST)*

273 We begin by comparing the absolute differences in the atmospheric “equilibrated” responses  
274 between the SSP 2-4.5 R and C members (Section 3a1-2) and between the 2- and 3xCO<sub>2</sub> simulations  
275 (Section 3a3). When interpreting these differences, however, it is important to note that these could  
276 partly be reflective of background differences in the CO<sub>2</sub> forcing. In particular, the CO<sub>2</sub> values in  
277 the SSP 2-4.5 extended experiments peak at 643 ppm, or roughly 2.4 times preindustrial values,

278 and decrease thereafter (Figure 1a in AR2023). It is perhaps not surprising, therefore, that this  
279 value of  $\text{CO}_2$  lies in between the  $2\times\text{CO}_2$  and  $3\times\text{CO}_2$  levels identified in Mitevski et al. (2021) as  
280 the transition point between the AMOC recovering and collapsing under abrupt forcing (Fig. 1b).

281 Given these differences in  $\text{CO}_2$  forcing (further exaggerated when considering the broader suite  
282 of  $1\text{-}5\times\text{CO}_2$  experiments) it may seem most natural to compare the simulations with respect to  
283 their associated instantaneous radiative forcing (RF) as in Mitevski et al. (2021). However, another  
284 difference between the transient SSP 2-4.5 and abrupt  $1\text{-}5\times\text{CO}_2$  experiments is the evolution of the  
285 forcing. As the AMOC is known to be sensitive to the time history of the forcing, this is important  
286 to take into consideration, and so we cast our scaling analysis in Section 3b (in which the SSP 2-4.5  
287 results are compared against the broader  $1\text{-}5\times\text{CO}_2$  suite) in terms of GMST. This approach is also  
288 more in spirit with Ceppi et al. (2018) as it directly addresses the extent to which the dynamical  
289 sensitivity captured in the simulations scales with equilibrium climate sensitivity (Q3).

290 Finally, a related but distinct approach is to normalize by annual mean GMST. KB2021 showed  
291 that doing so highlights large differences in temperature gradients and the zonal mean meridional  
292 circulation between models in which the AMOC weakens substantially ( $> 7$  Sv), compared to  
293 models showing a limited AMOC response ( $< 7$  Sv). However, while this approach is well suited  
294 to understanding the multi-model response to the same ( $4\times\text{CO}_2$ ) forcing, it does not directly afford  
295 insight into how dynamical sensitivity scales with GMST. As we have tried both normalizing and  
296 not normalizing in this study and draw generally very similar conclusions (not shown), we focus  
297 on the unnormalized results.

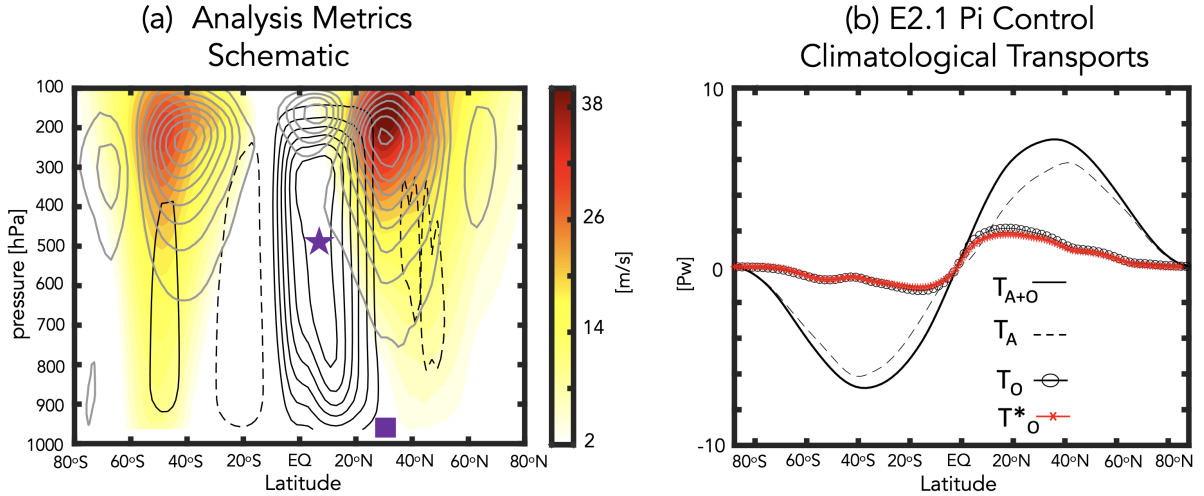
#### 298 *d. Analysis Approach*

##### 299 1) HADLEY CELL AND STORM TRACK DIAGNOSTICS

300 Whereas KB2021 focused on the latitude of the northern midlatitude jet, here we expand their  
301 analysis to also include measures of the Hadley Cell (HC) and the storm tracks. Figure 2a highlights  
302 how these measures of the HC and midlatitude jet are coupled through eddy momentum fluxes.

316 To quantify the characteristics of the Hadley Cell we use metrics calculated using the Tropical-  
317 width Diagnostics (TropD) code (Adam et al. (2018)) based on fields that were zonally and  
318 seasonally averaged before calculation of the metrics. The edge of the HC,  $\phi_{\text{UAS}}$ , is defined as the  
319 zero-crossing latitude of the surface zonal wind (corresponds to UAS in TropD and is calculated





303 FIG. 2. (a): Schematic of the main zonal mean dynamical metrics considered in this study, illustrated  
 304 using data from the preindustrial control simulation. The December-January-February (DJF) climatological  
 305 mean meridional circulation is shown in black contours, with solid and dashed lines denoting clockwise and  
 306 counterclockwise directions, respectively (contour interval:  $3 \times 10^{10}$  kg/s). The DJF zonally averaged zonal winds  
 307 are shown in the filled colored contours (only positive values shown; contour interval: 2 m/s) and the DJF eddy  
 308 momentum fluxes are shown in the grey contours (contour interval:  $8 \text{ m}^2/\text{s}^2$ ). The purple star denotes the  
 309 Northern Hemisphere (NH) Hadley Cell strength, or the maximum value of the mean meridional streamfunction  
 310 at 500 hPa equatorward of where it crosses zero, while the edge is denoted by  $\phi_{UAS}$  (purple square), or the zero-  
 311 crossing latitude of the surface zonal wind. (b): Annual mean meridional distributions of the total atmospheric  
 312 ( $T_A$ ; black dashed line) and combined atmosphere-ocean ( $T_{A+O}$ ; black solid line) northward energy transports  
 313 for the preindustrial control simulation. The implied ocean heat transport ( $T_O$ ; black circled line), calculated by  
 314 subtracting  $T_A$  from  $T_{A+O}$ , exhibits good agreed with online calculations of the ocean transports ( $T_O^*$ ; red starred  
 315 line). For more details see Section 2.

320 using the “zero-crossing” method) (Fig. 2a, purple square). This measure of the HC was shown  
 321 to correlate well with the latitude at which the mean meridional streamfunction at 500 hPa crosses  
 322 0 poleward of its tropical extremum (Vaugh et al. (2018)). The value of that tropical extremum  
 323 ( $\Psi_{500}$ ) is also examined as a measure of HC strength (Fig. 2a, purple star).

324 In addition to looking at the Hadley Cell, we also examine its relation to the northern midlatitude  
 325 jet via the eddy momentum fluxes. This is based on research showing a strong connection  
 326 between the evolution of the Hadley Cell and the latitude of the maximum eddy momentum fluxes

327 (Schneider (2006); Chemke and Polvani (2019); Menzel et al. (2019)). The eddy momentum fluxes  
 328 are calculated as in Chemke and Polvani (2019) as the time mean of  $[u'v']$ , where  $u$  and  $v$  are  
 329 the zonal and meridional winds, respectively, and primes represent deviations from both the zonal  
 330 and monthly means. In particular we are interested in the latitude where the eddy momentum  
 331 flux maximizes (eddy momentum convergence = 0) (Fig. 2a, grey contours). As it is well known  
 332 that the largest eddy momentum flux convergences are closely collocated with the extratropical  
 333 storm tracks (e.g., Lau et al. (1978), Lim and Wallace (1991)), we also examine the vertically  
 334 averaged eddy kinetic energy, calculated using daily output. Connections with static stability and  
 335 baroclinic eddy generation are also made, where the latter is quantified using  $\sim \alpha'\omega'$ , where primes  
 336 denote zonal deviations and  $\alpha$  and  $\omega$  refer to one over the density and vertical velocity in pressure  
 337 coordinates, respectively.

## 338 2) ENERGETIC ANALYSIS

339 To put the results of the dynamical analysis in an energetic context we evaluate the total meridional  
 340 heat transport of the coupled ocean-atmosphere transport system, further partitioned into its oceanic  
 341 and atmospheric contributions. Following Magnusdottir and Saravanan (1999) we estimate the  
 342 total vertically integrated atmospheric heat flux ( $T_A$ ) as:

$$\begin{aligned}
 \frac{\partial \cos \phi}{\partial \phi} \overline{[T_A]} &\equiv \frac{\partial \cos \phi}{\partial \phi} \int_1^0 \overline{(c_p T + gz + Lq) v \rho d\eta} \\
 &= \overline{[-F_T - F_S + SHF + LHF]} \quad (1)
 \end{aligned}$$

343 as well as the vertically integrated meridional heat flux in the combined atmosphere-ocean system  
 344 ( $T_{A+O}$ ) as:

$$\frac{\partial \cos \phi}{\partial \phi} \overline{[T_{A+O}]} \equiv \overline{[-F_T]} \quad (2)$$

345 where moist static energy density is the sum of dry static energy density ( $c_p T + gz$ ) and the latent  
 346 heat density ( $Lq$ ),  $\rho$  and  $v$  refer to the mass density and horizontal velocity on  $\eta$  surfaces. Zonal  
 347 averages and time averages are denoted by square brackets and overbars, respectively. The terms  
 348 on the RHS of both equations refer to energy fluxes out of the top of the atmosphere and at the

349 surface:  $F_T$  (net upward flux of radiation at the top of the atmosphere, calculated as outgoing  
350 longwave radiation (OLR) minus the absorbed solar radiation (ASR)),  $F_S$  (net downward flux of  
351 radiation at the surface equal to the sum of net downward longwave (LWF) and shortwave (SWF)  
352 radiation), and the fluxes of latent and sensible heat at the surface (LHF and SHF).

353 The resulting annual mean meridional distributions of  $T_A$  and  $T_{A+O}$ , calculated using the E2.1  
354 150-year preindustrial control simulation, is consistent with the climatological energy transports  
355 presented in other studies (e.g., Magnusdottir and Saravanan (1999), Held and Soden (2006))  
356 (Figure 2b). Note that the implied ocean heat transport, calculated by subtracting the first from  
357 the second equation above (Fig. 2b, black circled line) is found to exhibit good agreement with  
358 online calculations of the ocean transports (Fig. 2b, red starred line). These northward ocean heat  
359 transports, simulated in historical integrations using E2.1, have been shown to agree well with 1992-  
360 2011 estimates from the ECCO ocean state estimate (Figure 23 in Kelley et al. (2020)). Finally,  
361 in addition to examining the compensation between atmospheric and oceanic poleward transports,  
362 we also further partition  $T_A$  into its moist versus dry contributions using online calculations of the  
363 vertically integrated dry static energy and latent heat northward transports (Section 3c).

### 364 **3. Results**

365 We begin by contrasting the regional SSP 2-4.5 C and R responses in sea surface temperature,  
366 sea level pressure, precipitation and zonal winds (Section 3a1) and in the large-scale zonal mean  
367 circulation (Section 3a2). Then we compare the SSP 2-4.5 C-R differences to the responses in the  
368  $2\times\text{CO}_2$  and  $3\times\text{CO}_2$  simulations (Section 3a3), followed by a discussion of the full set of abrupt  
369  $1-5\times\text{CO}_2$  experiments, which we use to examine how the changes in thermodynamics and the  
370 circulation scale with changes in global mean surface temperature (Section 3b). To interpret the  
371 dynamical scaling results we then examine the compensation that arises between the ocean and  
372 atmosphere in response to a decline and eventual collapse of the AMOC (Section 3c).

373 *a. Equilibrated Responses*

374 1) SSP 2-4.5 COLLAPSED VS. RECOVERED: NEAR-SURFACE TEMPERATURES, PRECIPITATION AND  
375 WINDS

376 Figure 1 (bottom panels) shows the evolution of annual global mean surface temperature in the  
377 SSP 2-4.5 C and R members (Fig. 1c) and the abrupt CO<sub>2</sub> experiments (Fig. 1d). Comparing the  
378 collapsed versus recovered SSP 2-4.5 ensemble members reveals global cooling associated with a  
379 sustained collapse of the AMOC such that by the time that the AMOC has recovered in the SSP  
380 2-4.5 R members the annual mean global surface temperature is almost one degree warmer, relative  
381 to the SSP 2-4.5 C members. In the abrupt CO<sub>2</sub> simulations, the GMST change in the 3xCO<sub>2</sub>  
382 experiment is only ~0.6°C warmer than the 2xCO<sub>2</sub> simulation, reflective of a clear flattening of  
383 the warming trend after years ~60-70. Overall, the changes in GMST are 2.2°C, 2.8°C, 3.0°C,  
384 and 2.3°C for the 2xCO<sub>2</sub>, 3xCO<sub>2</sub> and SSP 2-4.5 recovered and SSP 2-4.5 collapsed ensembles,  
385 respectively.

386 That the cooling associated with a steady decline and eventual collapse of the AMOC acts to  
387 mitigate, and partially counteract, other components of the global surface temperature change is  
388 reflected in a non-monotonic change in equilibrium climate sensitivity that occurs between 2xCO<sub>2</sub>  
389 and 3xCO<sub>2</sub> over the broader range of experiments spanning 1-to-5xCO<sub>2</sub> (Figure 1 in Mitevski et al.  
390 (2021)). This counteracting of warming due to a weakening of the AMOC has also been shown to  
391 occur in 21<sup>st</sup> century warming simulations (Drijfhout et al. (2012), Caesar et al. (2018), Marshall  
392 et al. (2015)).

393 While the AMOC influence on the climate can occur via its changes in GMST, a reduction in  
394 AMOC strength can also influence sea surface temperature patterns. We examine this next, with a  
395 focus on DJF, and examine changes in SSTs and associated spatial gradients over the Atlantic and  
396 Pacific (Figure 3a). Note that a saturated color bar has been used in order to highlight the structure  
397 of SST changes outside of the North Atlantic region.

398 Examination of the North Atlantic reveals much more cooling in the SSP 2-4.5 collapsed simula-  
399 tions (Fig. 3a) over the subpolar North Atlantic (SPNA), consistent with the results from previous  
400 studies. This cooling within the SPNA region is also associated with a large increase in meridional  
401 SST gradients over the North Atlantic south of 40°N and enhanced zonal gradients between the

402 western and eastern Atlantic basins. There is also an indication of a slight increase in SST gradients  
403 in the tropics.

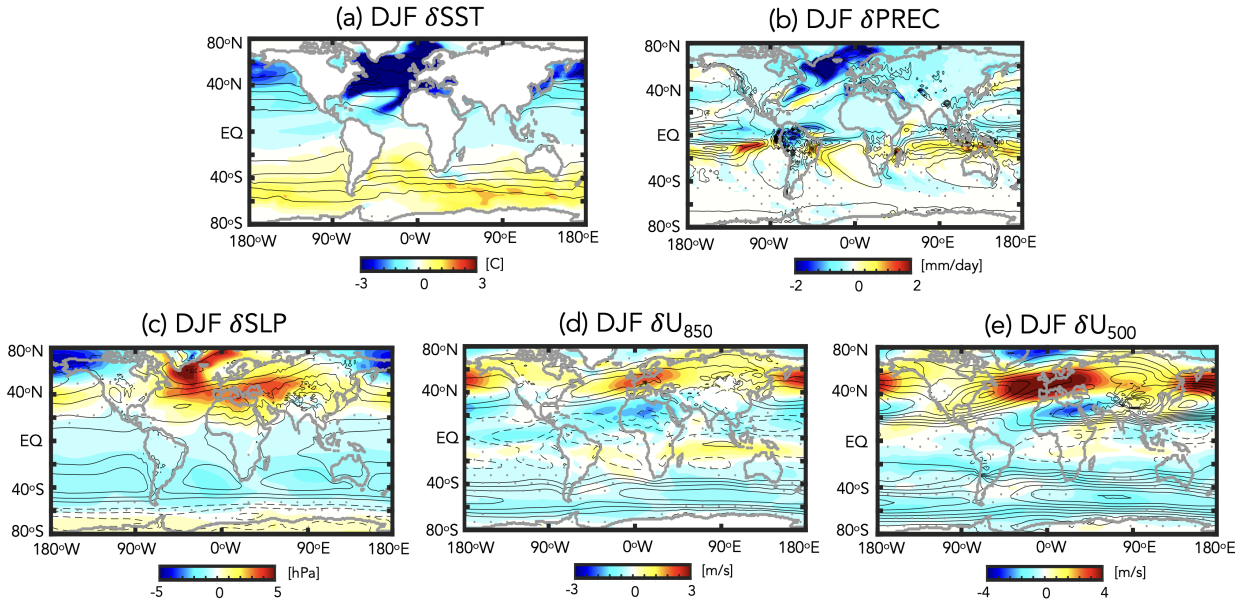
404 The cooler SSTs in the recovered simulations are not only confined to the Atlantic, but also  
405 span the Pacific (Fig. 3a), resulting in stronger meridional SST gradients, particularly over middle  
406 northern latitudes. Preliminary analysis of the evolution of the SST response (Appendix Figure  
407 1) shows that this cooling over the extratropical Pacific occurs over several centuries and may be  
408 related to a deepening and poleward shift of the Aleutian Low (Fig. 3c), resulting in more advection  
409 of colder temperatures over the West Pacific (Wu et al. (2008)), although direct thermodynamic  
410 advection of colder North Atlantic air may also be occurring. By comparison, the changes in SSTs  
411 and associated gradients in the tropical Pacific are much smaller. Unlike some previous studies  
412 (Timmermann et al. (2007), Zhang and Delworth (2005)) we find no evidence of an El Niño like  
413 response to an AMOC weakening, although the robustness of this response has recently been  
414 questioned (KB2021).

415 In the SH, SSTs warm over the extratropics in the SSP 2-4.5 collapsed integrations, compared  
416 to the simulations in which the AMOC recovers. This warming takes several centuries to develop  
417 (Appendix Figure 1) and resembles the evolution of the SST pattern documented in Pedro et al.  
418 (2018) (their Figure 7). This delayed warming over the SH results in increased SST gradients over  
419 the South Atlantic ( $\sim 60^\circ\text{S}$ ) in the SSP 2-4.5 C runs, relative to SSP 2-4.5 R, a feature which is not  
420 captured in the  $3\times\text{CO}_2$  simulation (discussed more in Section 3a3).

421 In addition to the changes in SSTs, the response in precipitation in the SSP 2-4.5 collapsed  
422 simulations reflects large decreases over the North Atlantic subpolar region, reductions over the  
423 Amazon and suggestions of a southward shift of the ITCZ over both the Atlantic and East Pacific  
424 basins (Fig. 3b). By comparison, the increased precipitation in the West Pacific is not statistically  
425 significant, consistent with previous studies (Vellinga and Wood (2008), KB2021).

426 Moving next to more dynamical measures, we examine changes in sea level pressure and near-  
427 surface zonal winds (Fig. 3c,d). The changes in sea level pressure show differences over the North  
428 Atlantic indicative of enhanced (anticyclonic) high level pressure over the subpolar latitudes in the  
429 runs in which the AMOC collapses (Fig. 3c). In addition to these SLP changes over the Atlantic,  
430 there is also a pronounced dipole of increased and reduced sea level pressure values over the North  
431 Pacific middle and high latitudes. While this response was not discussed in KB2021, earlier studies

## SSP 2-4.5 Collapsed - Recovered

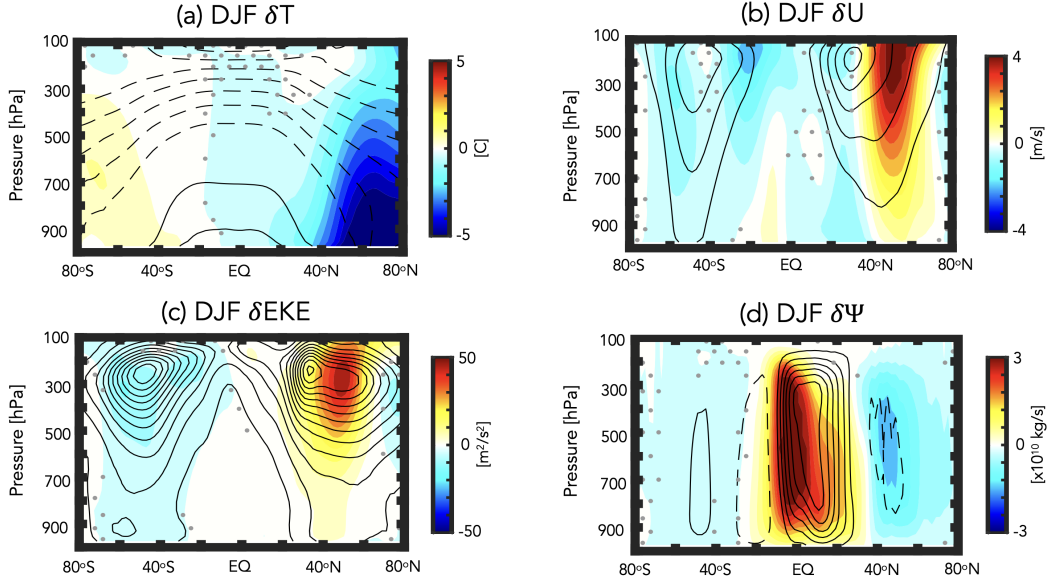


443 FIG. 3. The difference in the year DJF 2400-2500 climatological mean (a) sea surface temperatures ( $\delta$ SST),  
 444 (b) precipitation ( $\delta$ PREC), (c) sea level pressure ( $\delta$ SLP), (d) 850 hPa zonal winds ( $\delta$ U<sub>850</sub>) and (e) 500 hPa zonal  
 445 winds ( $\delta$ U<sub>500</sub>) between the SSP 2-4.5 collapsed (C) and recovered (R) ensemble members. Climatological mean  
 446 values from the preindustrial control simulation are denoted in the black contours (contour intervals: (a) 5°C,  
 447 (b) 2 mm/day, (c) 5 mb, (d) 3 m/s and (e) 3 m/s). Grey stippling denotes regions where the SSP 2-4.5 C-R  
 448 differences are not statistically significant.

432 have shown that a weakening of the AMOC is associated with a deepening of the Aleutian Low  
 433 (Wu et al. (2008), Liu et al. (2020)).

434 Consistent with the SLP changes over the North Pacific, there is a strong signature of a weakened  
 435 AMOC in the near surface zonal winds (850 hPa) (Fig. 3d). These wind changes over the Pacific  
 436 reflect a poleward shift of the midlatitude jet, whereas over the North Atlantic the jet mainly  
 437 accelerates and extends further eastward over Europe. This acceleration over the North Atlantic is  
 438 more pronounced in the mid-troposphere (Fig. 3e), as was also reported in KB2021, who identified  
 439 a statistically significant strengthening of the midlatitude jet at 250 hPa, but not at 850 hPa, in  
 440 models featuring a stronger AMOC decline. Finally, in contrast to the NH, there is a uniform  
 441 weakening of the zonal winds over the SH extratropics. We discuss the vertical coherence of these  
 442 wind changes in the next section.

## SSP 2-4.5 Collapsed - Recovered



449 FIG. 4. The difference in the year DJF 2400-2500 climatological mean zonal mean (a) temperature ( $\delta T$ ), (b)  
 450 zonal wind ( $\delta U$ ), (c) eddy kinetic energy ( $\delta EKE$ ) and (d) Eulerian mean stream function ( $\delta \Psi$ ) between the SSP  
 451 2-4.5 collapsed (C) and recovered (R) ensemble members. Climatological mean values from the preindustrial  
 452 control simulation are denoted in the black contours (contour intervals: (a)  $10^\circ\text{C}$ , (b)  $8\text{ m/s}$ , (c)  $28\text{ m}^2/\text{s}^2$  and  
 453 (d)  $3 \times 10^{10}\text{ kg/s}$ ). Note that in (d) solid and dashed lines denoting clockwise and counterclockwise directions,  
 454 respectively. Grey stippling denotes regions where the SSP 2-4.5 C-R differences are not statistically significant.

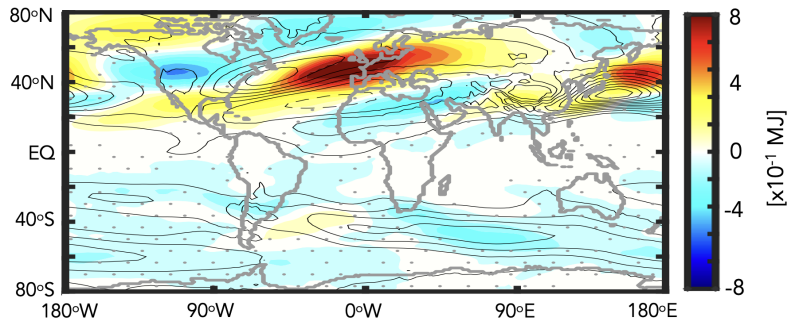
### 455 2) SSP 2-4.5 COLLAPSED VS. RECOVERED: VERTICAL STRUCTURE

456 In addition to its impacts on SSTs, changes in the AMOC impact the vertical structure of  
 457 meridional temperature gradients in the atmosphere. To interpret the zonal wind changes shown in  
 458 Figure 3 we therefore next examine the zonal mean changes in temperatures, zonal winds and eddy  
 459 kinetic energy, as well as their coupling to responses in the tropical mean meridional circulation  
 460 (Figure 4).

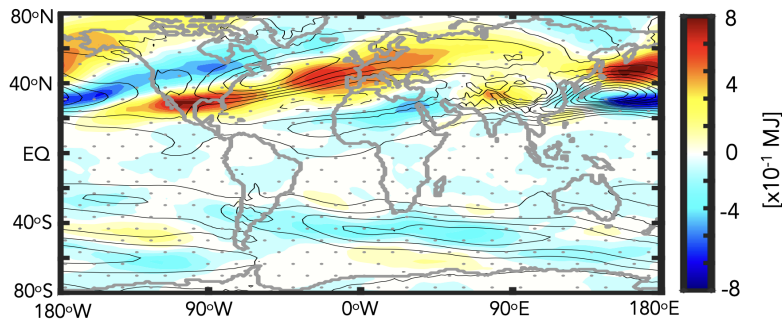
465 We begin by examining changes in temperature (Fig. 4a), which show much more cooling over  
 466 the NH high latitude troposphere in the SSP 2-4.5 collapsed runs. A similar reduction in Arctic  
 467 warming was reported in the “strongly” collapsed models examined in KB2021 (their Figure S5)  
 468 and in Liu et al. (2020) (their Figure 6). In addition to the changes over the northern extratropics,  
 469 we also find an indication of weak polar amplification characterized by warming throughout the

# DJF Eddy Kinetic Energy

(a) SSP 2-4.5 Collapsed - Recovered



(b)  $3\times\text{CO}_2 - 2\times\text{CO}_2$



461 FIG. 5. (a) The difference in the year DJF 2400-2500 climatological mean vertically integrated eddy kinetic  
462 energy between the SSP 2-4.5 C and R ensembles. (b) Same as in (a), except showing the year 120-150  
463 difference between the  $3\times\text{CO}_2$  and  $2\times\text{CO}_2$  integrations. Climatological mean values from the preindustrial  
464 control simulation are denoted in the black contours (contour interval:  $5\times 10^{-1}$  MJ).

470 SH middle and high latitudes poleward of  $40^\circ\text{S}$ , also seen in the SST differences (Fig. 3a).  
471 This warming in the SH is consistent with Liu et al. (2020) (their Figure 6), but inconsistent  
472 with KB2021, which likely reflects their focus on shorter (100-150 year) timescales. In addition,  
473 KB2021 also identified more warming in the tropical upper troposphere, a feature that is also  
474 not evident in the SSP 2-4.5 collapsed runs. Normalization of our results by GMST (not shown)  
475 produces an anomalous upper tropical tropospheric warming, suggesting that the results reported  
476 in KB2021 are reflective of the normalization performed in that study, not of absolute temperature  
477 differences.

478 Moving next to the zonal winds (Fig. 4b) we find that the reduced warming over NH high  
479 latitudes is associated with enhanced meridional temperature gradients, which result in a poleward

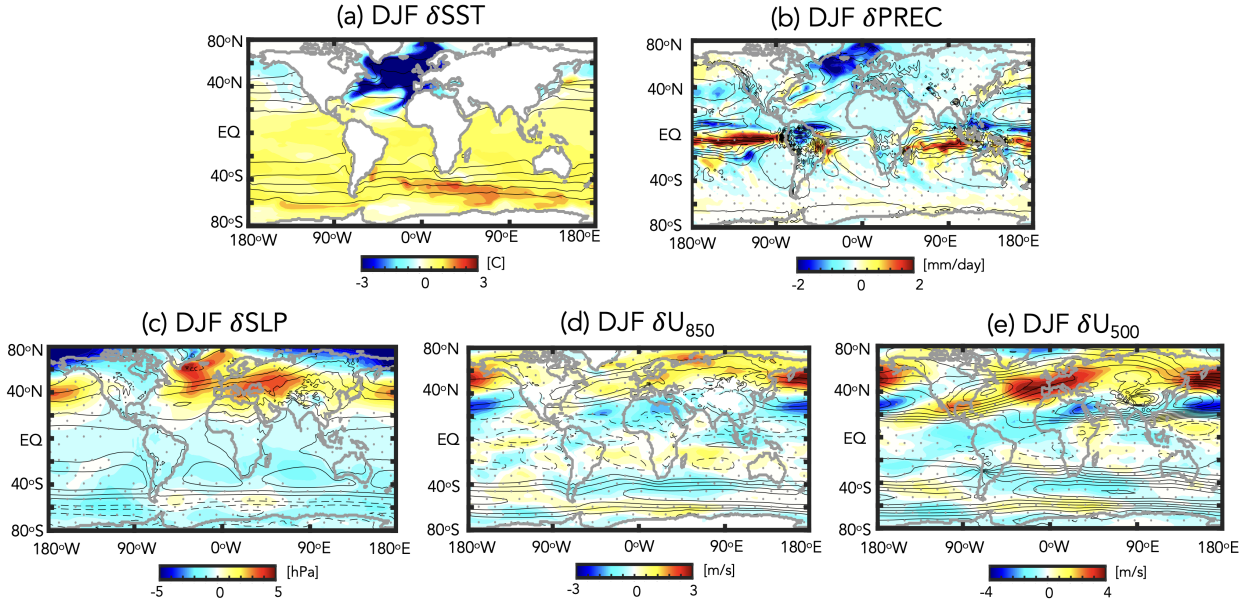


480 shift of the zonal mean northern midlatitude jet in response to a decline and eventual collapse of  
481 the AMOC. A similar poleward shift in the NH jet was documented in KB2021 (their Figure 4)  
482 and in Liu et al. (2020). In the SH the zonal winds weaken and, if anything shift equatorward, in  
483 the SSP 2-4.5 C ensemble members, consistent with the weak polar amplification in that region  
484 (Fig. 4a). Again, this wind response is highly consistent with Liu et al. (2020), but opposite  
485 to that shown in KB2021, who identified a poleward shift of the SH jet. As that study did not  
486 propose a testable mechanism for the SH jet changes, it is not entirely clear what is the driver of  
487 the differences between their results and those presented here and in Liu et al. (2020), although  
488 both the normalization by GMST as well as the differing integration lengths likely contribute.

489 In concert with the changes in the zonal winds, the changes in eddy kinetic energy (EKE) over  
490 the NH feature increases north of 40°N (Fig. 4c). Note that there is no statistically significant  
491 response in the subtropics and only the wind (and EKE) changes poleward of 40°N are robust.  
492 Zonally, the increases in EKE are concentrated over the North Atlantic and extend eastward over  
493 Europe, as well as over the West Pacific (Fig. 5a), strongly resembling the zonal wind changes  
494 at 500 hPa (Fig. 3e). Comparisons with the changes in EKE associated with an AMOC collapse  
495 in another model (the Community Earth System Model (CESM-LE)) examined in Mitevski et al.  
496 (2021) show very similar anomalies (not shown). Furthermore, a spectral decomposition of these  
497 NH EKE changes show increased wave energy over wavenumbers 1-6 in the collapsed SSP 2-4.5  
498 members, relative to the recovered members (also not shown).

501 Finally, the changes in the mean meridional stream function indicate an overall strengthening  
502 of the wintertime NH Hadley circulation in the collapsed SSP 2-4.5 simulations (Fig. 4d). This  
503 intensification of the NH Hadley circulation in response to an AMOC shutdown has been reported  
504 in previous studies (Zhang and Delworth (2005), Orihuela-Pinto et al. (2022)) and generally  
505 associated with a southward displacement of the ITCZ, although Brayshaw et al. (2009) also  
506 identify a zonally localized enhancement of the Hadley Cell region over the subtropical Atlantic,  
507 which they associate with increased meridional SST gradients in that region. Compared to those  
508 studies, however, our results also show a poleward displacement of the northern Hadley Cell edge  
509 in the lower troposphere (>500 hPa), a result which has not been directly commented on in the  
510 literature. These stream function anomalies over the NH extratropical lower troposphere appear to  
511 be coupled to a slight strengthening and poleward displacement of the northern Ferrel cell.

## 3xCO<sub>2</sub> – 2xCO<sub>2</sub>



499 FIG. 6. Same as Figure 3, except showing the difference between the year 120-150 climatological mean 3xCO<sub>2</sub>  
500 and 2xCO<sub>2</sub> responses.

### 512 3) COMPARISON WITH 2xCO<sub>2</sub> vs 3xCO<sub>2</sub>

513 Comparisons of the surface and lower tropospheric impacts associated with an AMOC collapse  
514 in the SSP 2-4.5 ensemble (Fig. 3) are highly consistent with the responses moving from 2xCO<sub>2</sub>  
515 to 3xCO<sub>2</sub> (Fig. 6). In particular, over the North Atlantic the changes moving from 2xCO<sub>2</sub> to  
516 3xCO<sub>2</sub> reflect cooler SSTs (Fig. 6a), reduced precipitation (Fig. 6b) and an anomalous anticyclonic  
517 circulation over the North Atlantic subpolar gyre region (Fig. 6c), as well as a strengthening and  
518 eastward extension of the North Atlantic jet over Europe (Fig. 6d, 6e). The magnitudes of the  
519 3xCO<sub>2</sub> changes are also similar to the responses in the SSP 2-4.5 collapsed ensemble members,  
520 albeit somewhat smaller (Fig. 3).

521 Though the overall responses in the surface temperatures and winds are very similar, there are  
522 some important differences worth noting. First, the SSTs in the 3xCO<sub>2</sub> simulation show much less  
523 cooling over the Pacific northern midlatitudes (> 40°N) compared to the SSP 2-4.5 C simulations,  
524 which likely reflects differences in the length of these integrations as this cooling takes centuries  
525 to equilibrate (Appendix Figure 1). Second, in response to 3xCO<sub>2</sub> there is more warming over the

526 NH subtropics and tropics, consistent with the higher CO<sub>2</sub> forcing in that simulation. Thus, unlike  
527 what happens in the SSP 2-4.5 C ensemble members, there is no SH polar amplification occurring  
528 at 3xCO<sub>2</sub>.

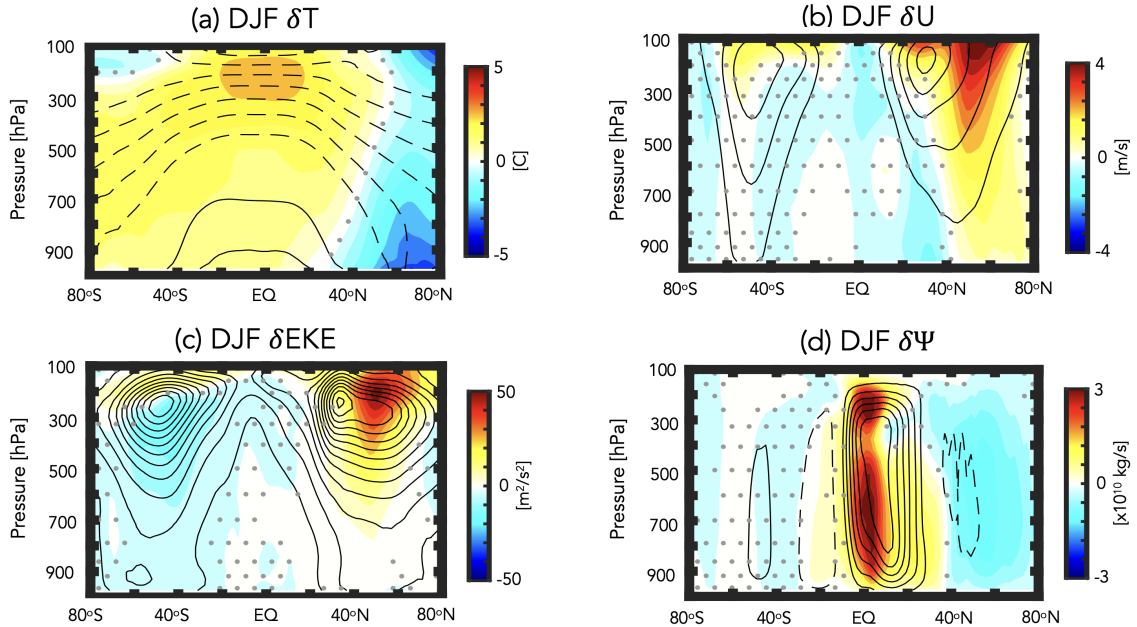
529 The different SST gradients over the northern high latitude Pacific and tropics and SH occurring  
530 at 3xCO<sub>2</sub> have implications for the jet and precipitation changes in these regions. In particular,  
531 over the Pacific northern midlatitudes, where there is much less cooling compared to the SSP 2-4.5  
532 C integrations, the jet response resembles more of a poleward shift, characterized not only by an  
533 acceleration north of 40°N, but also reduced winds ~20°N; in the tropical Pacific there is also a  
534 much stronger increase in precipitation, relative to the AMOC SSP 2-4.5 C ensemble.

535 Even over the North Atlantic the SST cooling is slightly weaker and less expansive and the jet  
536 response at 850 hPa is not statistically significant at 3xCO<sub>2</sub>, in contrast to the SSP 2-4.5 collapsed  
537 ensemble members. In the SH, there is also a suggestion of a poleward shift of the midlatitude jet  
538 at 3xCO<sub>2</sub>, not evident in the SSP 2-4.5 C integrations, although these changes are not statistically  
539 significant. These subtle differences aside, however, the overall similarities between Figures 3 and  
540 6 are remarkable and suggest that the climate response that occurs moving from 2xCO<sub>2</sub> to 3xCO<sub>2</sub>  
541 is, to first order, determined by the changes in AMOC strength.

542 Strong consistency is also found when comparing the vertical response of the large-scale cir-  
543 culation between the AMOC SSP 2-4.5 collapsed ensemble (Fig. 4) and the 3xCO<sub>2</sub> integration  
544 (Fig. 7). That is, in concert with stronger cooling over the Arctic (Fig. 7a), the 3xCO<sub>2</sub> simulation  
545 features a stronger poleward shift of the NH zonal mean jet (Fig. 7b), increased EKE northward of  
546 40°N (Fig. 7c) and a strengthened Hadley Cell (Fig. 7d).

547 One difference in vertical structure occurs over the Arctic, where the cooling that occurs at 3xCO<sub>2</sub>  
548 (Fig. 7a) is much smaller than in the collapsed SSP 2-4.5 ensemble (Fig. 4a), reflecting the higher  
549 CO<sub>2</sub> forcing in that simulation. There is also stronger warming occurring within the tropics and  
550 over southern latitudes. Despite these differences in absolute temperature, however, the increase in  
551 meridional temperature gradients that occurs is similar to what happens when comparing the SSP  
552 2-4.5 C and R ensemble members. As such, the zonal mean NH jet response is quite similar in the  
553 3xCO<sub>2</sub> simulation (Fig. 7b) compared to SSP 2-4.5 C (Fig. 4b) and is also coupled to an EKE  
554 increase on the poleward flank of the jet (Fig. 7c). Maps of the EKE response show that at 3xCO<sub>2</sub>  
555 much of this increased EKE reflects changes over the Atlantic (Fig. 5b), as in the SSP 2-4.5 C en-

## $3xCO_2 - 2xCO_2$



558 FIG. 7. Same as Figure 4, except showing the difference between the year 120-150 climatological mean  $3xCO_2$   
 559 and  $2xCO_2$  responses.

556 semple (Fig. 5a), although there is also increased EKE over the western Pacific and North America.  
 557

560 To summarize: In response to a collapse of the AMOC, our results show widespread cooling over  
 561 the Arctic and stronger meridional temperature gradients over the NH. This increase in temperature  
 562 gradients is associated with a poleward shift of the midlatitude jet (and associated eddy energy)  
 563 as well as a strengthening of the NH Hadley Cell. In the lower troposphere ( $> 600$  hPa) the NH  
 564 Hadley cell is displaced poleward.

565 Over the Northern Hemisphere the response to an increase from  $2xCO_2$  to  $3xCO_2$  is remarkably  
 566 similar to the differences between the SSP 2-4.5 R and C simulations, in terms of both the magnitude  
 567 and spatial patterns of these changes. Some exceptions, however, include the near surface (850  
 568 hPa) wind response over the North Atlantic, which is not statistically significant at  $3xCO_2$ , as  
 569 well as in the tropics, where precipitation increases strongly over the Pacific. There is also more  
 570 warming in the tropical upper troposphere and SH in the  $3xCO_2$  simulation. Overall, this close

571 correspondence suggests that the collapse of the AMOC is the dominant driver of the large-scale  
572 circulation changes moving from 2xCO<sub>2</sub> to 3xCO<sub>2</sub> in our model.

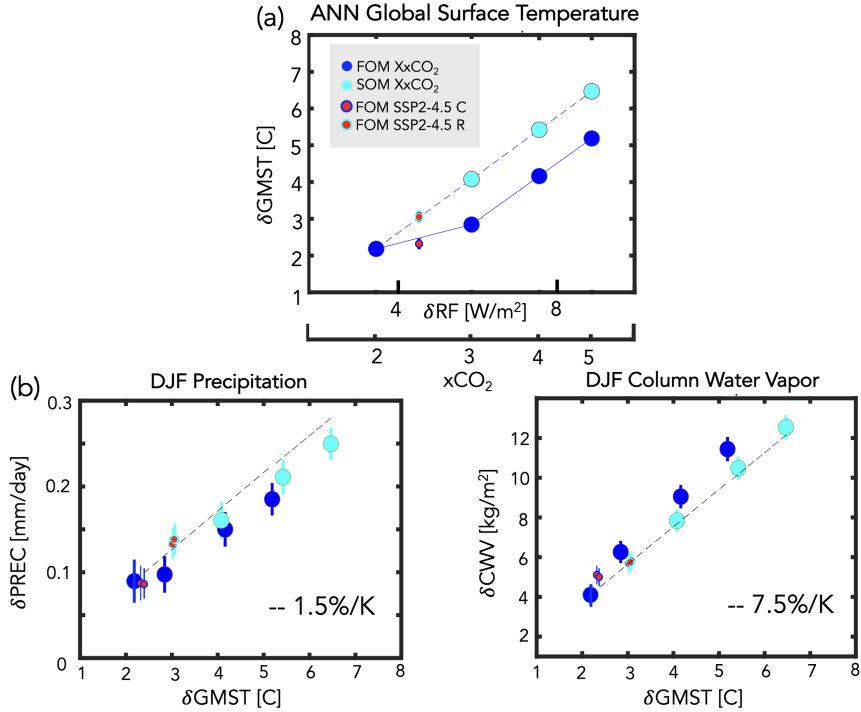
573 *b. Scaling of Equilibrated Thermodynamic and Dynamic Responses with Global Mean Surface*  
574 *Temperature (GMST)*

575 One question (Q3) not addressed in the previous sections relates to how changes in the climate  
576 response to an eventual collapse of the AMOC scale with changes in GMST. To this end, here we  
577 expand our analysis to include the results of additional (4xCO<sub>2</sub> and 5xCO<sub>2</sub>) FOM abrupt CO<sub>2</sub> runs,  
578 as well as the results from the SOM abrupt CO<sub>2</sub> integrations.

579 1) GLOBAL THERMODYNAMIC CHANGES

580 Figure 8a shows the annual global mean surface temperature response among all of the sim-  
581 ulations, plotted as a function of associated instantaneous radiative forcing (RF), where RF is  
582 calculated from the expression  $5.35 \ln(NxCO_2/1xCO_2)$  (Byrne and Goldblatt (2014)) and, for each  
583 run, N is the CO<sub>2</sub> multiple of the PI value (2.4, for the case of all SSP 2-4.5 ensemble members).  
584 The changes in GMST across this broader range of CO<sub>2</sub> forcing show the nonlinear behavior  
585 between the 2xCO<sub>2</sub> and 3xCO<sub>2</sub> FOM simulations (blue circles) that was first identified in Mitevski  
586 et al. (2021) (their Figure 1). By comparison, the results from the SOM experiments (aqua circles)  
587 show no evidence of a nonlinearity. This result was also documented in Mitevski et al. (2021) and  
588 suggests that the changes in ocean horizontal and vertical heat fluxes not included in the q-flux  
589 experiments are primarily responsible for the nonlinear changes in GMST occurring in the FOM  
590 experiments.

603 Building on Mitevski et al. (2021), here we also include the results from the SSP 2-4.5 R and C  
604 ensemble members (red circles, cyan and blue outlines) which are seen to align respectively with the  
605 SOM (solid cyan) and FOM (solid blue) scalings. This suggests that the GMST differences between  
606 the collapsed (C) versus recovered (R) SSP 2-4.5 ensemble members are primarily associated with  
607 the changes in ocean heat convergence occurring in the former. Note that the SSP 2-4.5 results are  
608 plotted with respect to the peak CO<sub>2</sub> level achieved (i.e. 643 ppm), which occurs at year 2200 (not  
609 at the values occurring during years 2400-2500, which are lower (579-598 ppm)) (Meinshausen  
610 et al. (2020)).



591 FIG. 8. Top: Changes in annual mean global mean surface temperature (GMST), plotted as a function of the  
 592 associated radiative forcing (RF), calculated from the expression  $5.35\ln(Nx\text{CO}_2/1x\text{CO}_2)$  (Byrne and Goldblatt  
 593 (2014)) where, for each run,  $N$  is the  $\text{CO}_2$  multiple of the PI value (2.4, for the case of the SSP 2-4.5 ensemble  
 594 members), consistent with the presentation in Mitevski et al. (2021). Bottom: Changes in DJF global mean  
 595 precipitation (left) and atmospheric column water vapor (right). Changes in precipitation and column water  
 596 vapor are plotted relative to the annual mean GMST changes in (a). Results from the abrupt 2-5 $\times\text{CO}_2$  fully  
 597 coupled atmosphere-ocean model (FOM) and slab ocean model (SOM) results are shown in the blue and cyan  
 598 filled circles. The FOM SSP 2-4.5 recovered (R) and collapsed (C) results are also shown in the red circles  
 599 (cyan and blue outlines, respectively). Interannual variability for each metric is indicated by the vertical bars.  
 600 Note that in all panels the SOM 2 $\times\text{CO}_2$  results have been adjusted to match the FOM 2 $\times\text{CO}_2$  results in order to  
 601 facilitate comparison of the FOM and SOM scalings with  $\text{CO}_2$  and GMST, not on the absolute magnitude of the  
 602 responses.

611 Next we examine how changes in first-order thermodynamic variables scale with these (nonlinear)  
 612 changes in GMST. As with GMST, the changes in global mean precipitation and integrated column  
 613 water vapor (CWV) also vary nonlinearly with respect to radiative forcing in the FOM simulations  
 614 moving from 2 $\times\text{CO}_2$  to 3 $\times\text{CO}_2$  (Appendix Figure 2). As expected from the GMST changes, this

615 behavior is absent in the SOM integrations and the SSP 2-4.5 C and R members again align with  
616 the FOM and SOM scalings, respectively.

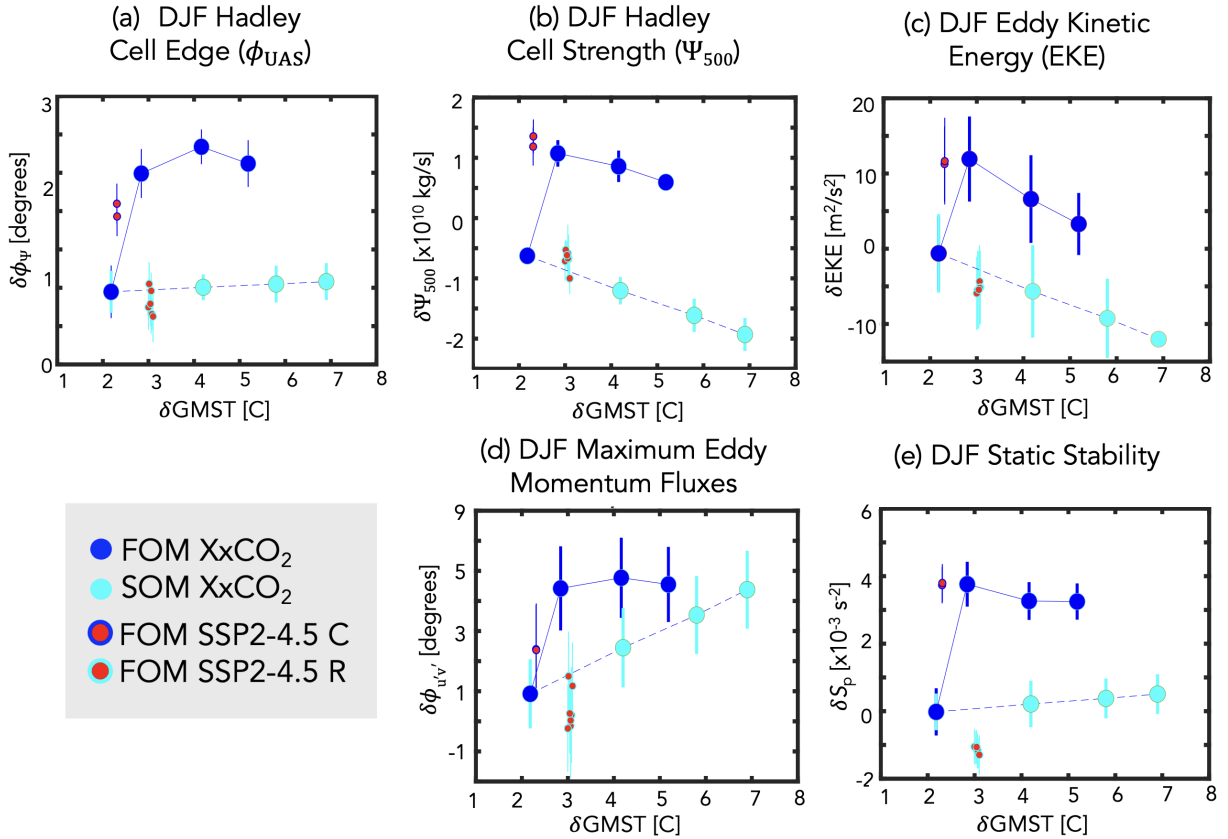
617 However, plotting the precipitation and CWV DJF changes relative to annual mean GMST,  
618 reveals that the nonlinear scaling with RF more-or-less disappears (Fig. 8b). This demonstrates  
619 that, while the first order global scale hydrological cycle is sensitive to the collapse of the AMOC,  
620 this sensitivity occurs primarily through changes in GMST. It is also interesting to note that  
621 the lower precipitation values occurring in the SOM integrations, for a given values of GMST,  
622 are consistent with the direct effect of greenhouse gases, which tend to suppress global mean  
623 precipitation (Samset et al. (2016)).

624 Finally, we note that the scaling of precipitation and CWV with GMST roughly follow the predic-  
625 tions from Held and Soden (2006), who identified a Clausius-Clapeyron (CC) scaling of integrated  
626 column water vapor (dashed black line denoting 7.5%/K, Fig. 8b, right) and a significantly sub-CC  
627 scaling of global mean precipitation (1.5%/K, Fig. 8b, left). While some additional nonlinearity  
628 in precipitation is also evident at higher CO<sub>2</sub> levels, as this is not immediately relevant to the SSP  
629 2-4.5 ensemble, we reserve further discussion for future work.

## 630 2) NORTHERN HEMISPHERE DYNAMICAL CHANGES: A REGIME SHIFT

631 Moving next to the dynamical response, we find that several measures of the NH DJF zonal mean  
632 dynamical circulation behave nonlinearly (and even non-monotonically) with respect to radiative  
633 forcing in the FOM simulations (Appendix Figure 3). Unlike precipitation and CWV, however, this  
634 non-linear behavior in the NH surface wind-based Hadley cell edge (Fig. 9a), Hadley Cell strength  
635 (Fig. 9b), northern midlatitude EKE (Fig. 9c), latitude of maximum eddy momentum fluxes (Fig.  
636 9d) and northern midlatitude static stability (Fig. 9e) also occurs after plotting as a function of  
637 GMST. Overall, these results suggest that there is no clear (certainly not linear) relationship between  
638 the northern Hadley Cell (strength and lower tropospheric edge) and midlatitude jet behavior with  
639 GMST in simulations ((<sub>i</sub>)3xCO<sub>2</sub> and SSP 2-4.5 C) in which the AMOC eventually collapses.

640 Rather, the changes in both the NH Hadley Cell edge and strength reflect an abrupt poleward shift  
641 and increase, respectively, moving from 2xCO<sub>2</sub> to 3xCO<sub>2</sub> and between the SSP 2-4.5 R and SSP  
642 2-4.5 C ensemble members. This abrupt poleward shift and strengthening saturates at 3xCO<sub>2</sub> and  
643 even decreases at higher CO<sub>2</sub> values for certain metrics, despite continued increases in GMST (Fig.



640 FIG. 9. Changes in various DJF Northern Hemisphere (NH) dynamical metrics, plotted as a function of GMST.  
 641 Specifically, shown are the Hadley Cell edge ( $\phi_{UAS}$ ) (a), Hadley Cell strength ( $\Psi_{500}$ ) (b), NH column eddy  
 642 kinetic energy (EKE) (c), latitude of the maximum NH eddy momentum fluxes (d) and NH midlatitude dry static  
 643 stability (e). The quantities in (a), (b) and (d) are defined in Section 2, while the zonally averaged EKE and static  
 644 stability changes have both been averaged over 300-1000 hPa and 30°N-60°N. Results from the abrupt 2-5xCO<sub>2</sub>  
 645 fully coupled atmosphere-ocean model (FOM) and slab ocean model (SOM) results are shown in the blue and  
 646 cyan filled circles. The FOM SSP 2-4.5 recovered (R) and collapsed (C) ensemble members are shown in the red  
 647 circles (cyan and blue outlines, respectively). Interannual variability for each metric is indicated by the vertical  
 648 bars. As in Figure 8 the SOM 2xCO<sub>2</sub> results have been adjusted to match the FOM 2xCO<sub>2</sub> results.

653 9b, 9c). As such, this saturation in the NH circulation is indicative of a “regime” shift in our model,  
 654 consistent with the use of the term in Caballero and Langen (2005), albeit for the low-gradient,  
 655 high temperature regime identified in their study using a more idealized model (see discussion in  
 656 Section 4). In particular, our results suggest that the AMOC collapse is associated with a regime  
 657 shift in our model between a climate state in which the Hadley Cell is substantially weaker and



658 displaced equatorward (strong AMOC) and a state in which the Hadley Cell and midlatitude EKE  
659 is stronger and displaced poleward (weak AMOC).

660 Note that, while the increases in Hadley Cell strength (Fig. 9b) have been well documented, the  
661 poleward shift in the northern Hadley Cell edge has been less examined (Fig. 9a). Our examination  
662 of the Hadley Cell edge, as gauged using the surface zonal winds, is partly motivated by the  
663 results presented in Figure 3d, which show increased SLP over the North Pacific and Atlantic high  
664 latitudes. That is, the SLP increases over the North Atlantic extend as far south as 40°N and  
665 thus, together with the Pacific response, reflect a pattern which is consistent with the SLP pressure  
666 signature of an expanded northern edge of the Hadley cell (Schmidt and Grise (2017)). Another  
667 motivation comes from KB2021, who suggest that, in addition to reduced warming over the Arctic,  
668 stronger tropical heating and a related expansion of the HC may contribute to the poleward shift of  
669 the northern jet, although this was never explicitly shown.

670 The fact that changes in the Hadley Cell and midlatitude eddy-driven jet are linked is consistent  
671 with recent studies showing that the HC edge is strongly linked to the latitude of maximum eddy  
672 momentum fluxes, such that a poleward shift of the jet is associated with HC expansion (Chemke  
673 and Polvani (2019), Waugh et al. (2018), Menzel et al. (2019)). As discussed in those studies,  
674 this connection is likely associated with changes in the latitude of the maximum eddy momentum  
675 fluxes and the vertical potential temperature gradient (i.e., the static stability,  $S_p = -\left(\frac{T}{\Theta}\right)\left(\frac{\partial\Theta}{\partial P}\right)$ ) over  
676 northern midlatitudes, which also exhibit regime shifts in the NH (Fig. 9 d-e). The sensitivity of  
677 the extratropical tropospheric eddy response to even modest changes in isentropic slope, resulting  
678 both from changes in baroclinicity and static stability, is well known (Thompson and Birner  
679 (2012)) and previous studies have shown that increases in static stability at higher CO<sub>2</sub> forcing  
680 can increase subtropical baroclinicity, causing the HC edge and subtropical eddy fields to shift  
681 poleward (Chemke and Polvani (2019); Menzel et al. (2019)). Note that the changes in EKE and  
682 static stability are shown averaged over 300-1000 hPa and over 30°N-60°N; similar results are  
683 found averaging over the entire hemisphere poleward of 20°N.

684 Another interesting feature highlighted in Figure 9 is that for some variables even the *sign* of the  
685 response is different than would otherwise be predicted from the SOM experiments which ignore  
686 changes in ocean heat convergence. This applies both to the changes in Hadley Cell strength (Fig.  
687 9b) and tropospheric column averaged EKE (Fig. 9c) which otherwise decrease in response to

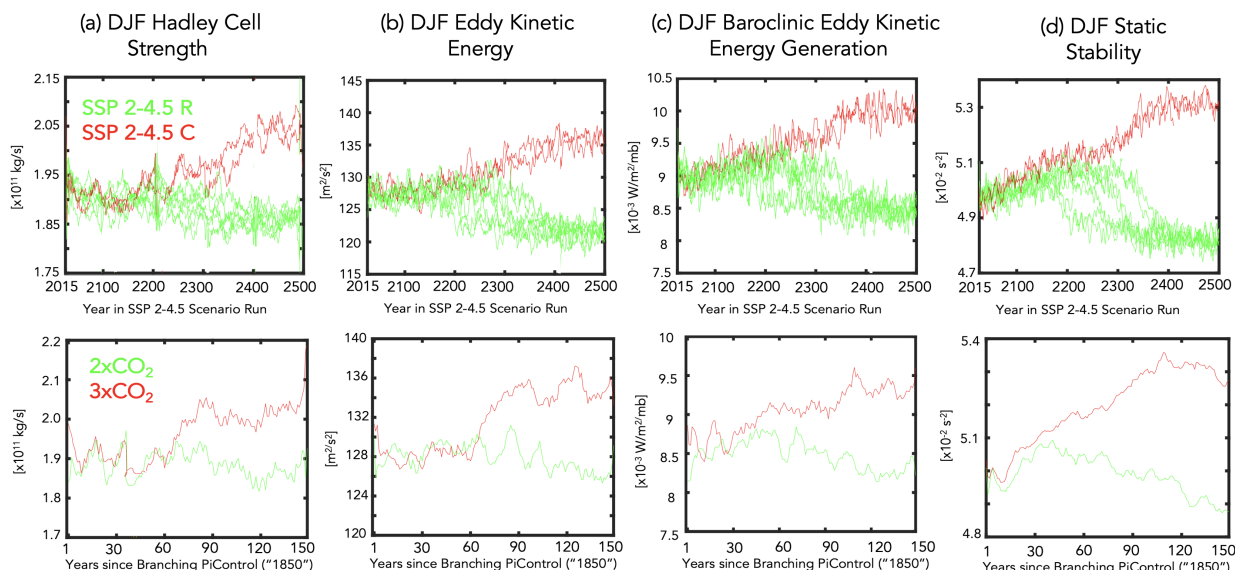
688 increasing CO<sub>2</sub>. This role of the ocean in the behavior of projected changes in northern EKE is  
689 consistent with Chemke et al. (2022), who showed that changes in ocean heat convergence are  
690 essential for correctly capturing the sign of the projected response in future storm track changes  
691 over the North Atlantic.

692 To further relate the changes in the Hadley Cell to the changes in midlatitude eddies, Figure 10  
693 shows the evolution of the response in northern HC strength (a), EKE (b), baroclinic eddy generation  
694 (c), and midlatitude static stability (d). While the HC strengthening may be more directly linked to  
695 the southward shift of the ITCZ as proposed in previous studies (Zhang et al. (2010)), the increases  
696 in dry static stability in the 3xCO<sub>2</sub> and SSP 2-4.5 C simulations evolve on a similar time scale as the  
697 changes in northern midlatitude tropospheric baroclinic eddies. The similar behavior among those  
698 variables suggests that they are mechanistically related. Furthermore, while changes in tropopause  
699 height have also been invoked to interpret future changes in the midlatitude jet stream (Cronin and  
700 Jansen (2016), Held (1993), Vallis et al. (2015)) and edge of the Hadley Cell (Lu et al. (2007)),  
701 we do not observe a consistent response in tropopause height between the 3xCO<sub>2</sub> and SSP 2-4.5  
702 C integrations (not shown), suggesting that tropopause height changes alone are not the primary  
703 drivers of the Hadley Cell and jet behaviors exhibited in these runs.

704 Note that the similar evolution of the HC strength and midlatitude eddy changes suggested in  
705 Figure 10 may seem at odds with the findings in Menzel et al. (2019), who showed a strong  
706 disconnect between the strength of the subtropical jet and the edge of the Hadley Cell. However,  
707 there are some subtle differences in the evolution of those responses; furthermore, that study  
708 inferred this disconnect based on interannual variability and the response to an abrupt 4xCO<sub>2</sub>  
709 forcing, which both yield a weakening and poleward shift of the Hadley Cell. By comparison, in  
710 connection with a southward shifted ITCZ a collapse of the AMOC is associated with a strengthened  
711 Hadley Cell (Zhang and Delworth (2005); Orihuela-Pinto et al. (2022)).

### 712 *c. Energetic Analysis: Bjerknes Compensation in Response to an AMOC Shutdown*

713 The previous section showed that, unlike the global mean thermodynamic response, several  
714 measures of NH dynamical sensitivity do not scale linearly with changes in global mean surface  
715 temperature. Rather, a collapsed AMOC in our model is accompanied by an abrupt strengthening  
716 and northward shift of the Hadley Cell and northern midlatitude jet. To better understand why these



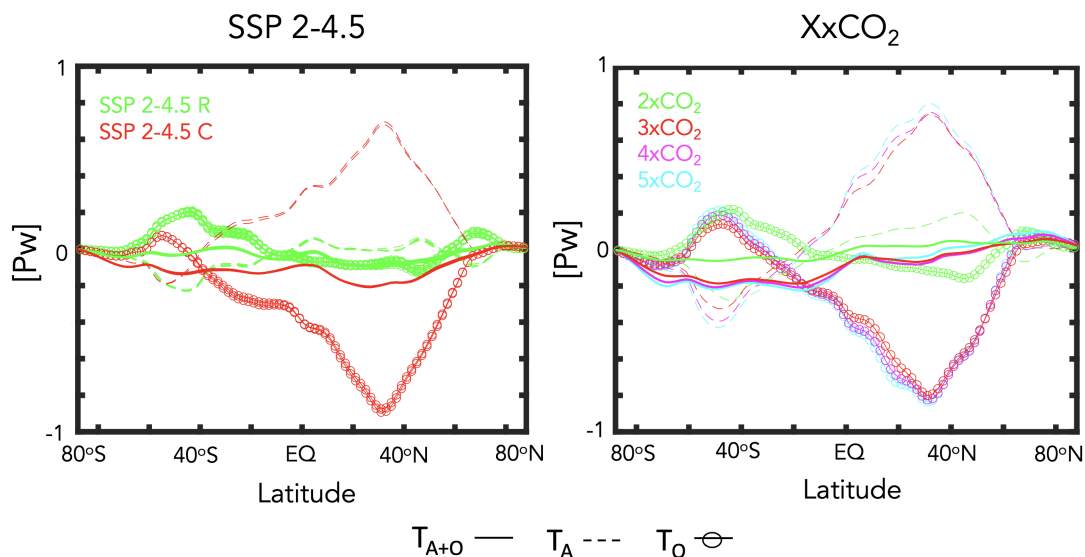
720 FIG. 10. Evolution of DJF Northern Hemisphere Hadley Cell strength (a), eddy kinetic energy (b), baroclinic  
 721 eddy kinetic energy generation (c) and midlatitude dry static stability (d). The baroclinic eddy generation has been  
 722 averaged over the same region (300-1000 hPa, 30°N-60°N) as the EKE and static stability fields, consistent with  
 723 Figure 9. Comparisons among the SSP 2-4.5 recovered (R) and collapsed (C) ensemble members (top panels)  
 724 and between the 2xCO<sub>2</sub> and 3xCO<sub>2</sub> runs (bottom panels) are shown in the green and red lines, respectively. A  
 725 5-year moving average has been applied to all time series.

717 variables exhibit this regime shift we examine the changes in energetics – and their partitioning  
 718 between the atmosphere and ocean – that arise moving from 2xCO<sub>2</sub> to 3xCO<sub>2</sub> and between the  
 719 SSP 2-4.5 R and SSP 2-4.5 C members.

## 726 1) OCEAN AND ATMOSPHERE COMPENSATION

727 Figure 11 shows the response in the annual mean northward total (atmosphere + ocean), oceanic  
 728 and atmospheric transports, relative to the preindustrial control simulation. Between 2xCO<sub>2</sub> and  
 729 3xCO<sub>2</sub> and between the SSP 2-4.5 R and SSP 2-4.5 C members there is a large decrease/increase  
 730 in  $T_O/T_A$  over northern latitudes with a peak located at ~30-40°N. This behavior is reflective of an  
 731 abrupt Bjerknes compensation that emerges in the model, wherein large anomalies in heat trans-  
 732 ported by the atmosphere increase to approximately balance large reductions in northward ocean  
 733 transport (Bjerknes (1964)). More precisely, the reduction in northward ocean heat transport in  
 734 the SSP 2-4.5 C ensemble members and at 3xCO<sub>2</sub> is approximately 1 PW (Fig. 11), representing

## Annual Mean Response in Poleward Heat Transport



741 FIG. 11. Changes in the annual mean atmospheric ( $T_A$ ), oceanic ( $T_O$ ) and total (atmospheric + oceanic,  $T_{A+O}$ )  
 742 northward energy transport, relative to the preindustrial control simulation. Results from the SSP 2-4.5 ensemble  
 743 members and the 2-5xCO<sub>2</sub> simulations are shown in the left and right panels. The simulations in which the  
 744 AMOC collapses (3xCO<sub>2</sub>, SSP 2-4.5 C) versus recovers (2xCO<sub>2</sub>, SSP 2-4.5 R) are highlighted in the red and  
 745 green lines, respectively.

735 a ~50% decrease relative to preindustrial values (Fig. 2b). Magnusdottir and Saravanan (1999)  
 736 attributed this compensatory response in the atmosphere to high dynamical efficiency of atmo-  
 737 spheric eddy transport. Note that the annual mean is shown here to facilitate comparison with the  
 738 annual mean results presented in previous studies (e.g., Figure 1 in Zhang and Delworth (2005)  
 739 and Figure 5 in Zhang et al. (2010)). We note in passing that the responses in the boreal winter  
 740 transports look very similar (not shown).

746 What Figure 11 makes clear is that the changes in ocean heat transport are dominated by the  
 747 changes in the AMOC, as reflected in the magnitude of the compensation occurring at 3xCO<sub>2</sub>  
 748 (similar to the compensation occurring in the SSP 2-4.5 C ensemble) which saturates, despite  
 749 further increases in CO<sub>2</sub> (and GMST). This helps to explain the behavior of the dynamical indices  
 750 discussed in the previous section (Fig. 9), which also saturate at 3xCO<sub>2</sub> and do not increase  
 751 (rather, decrease) moving to higher CO<sub>2</sub> forcings. A dramatic reduction in poleward ocean heat

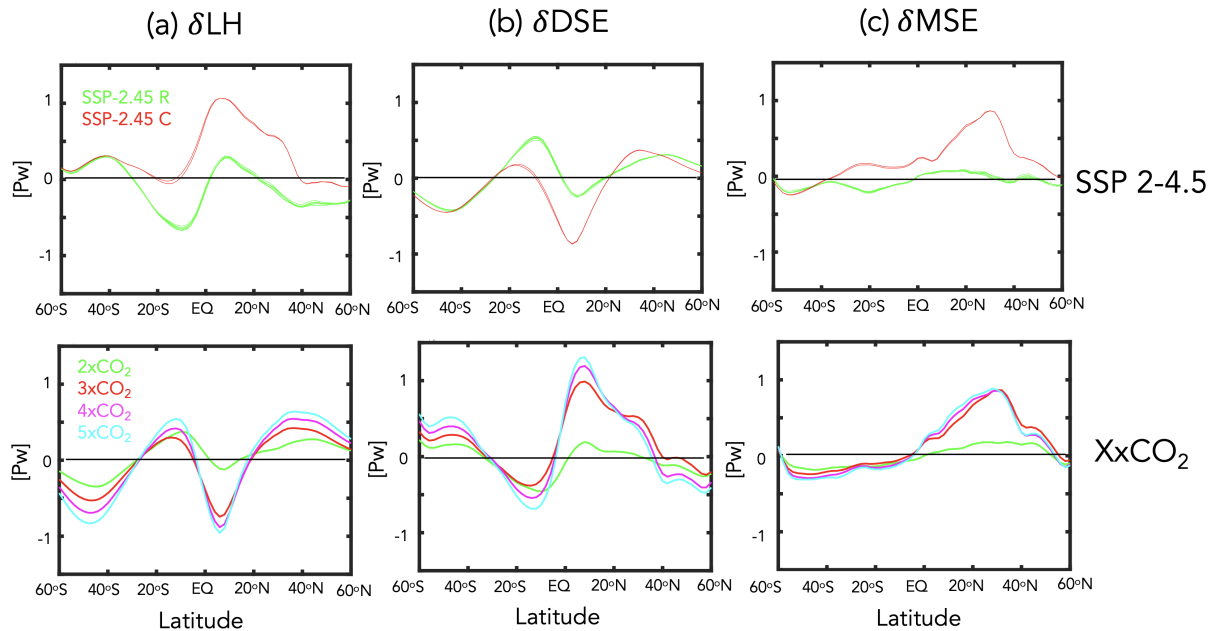
752 transport at  $\sim 30\text{-}40^\circ\text{N}$  was also noted in the CMIP5 historical models in association with strong  
753 air-sea interactions within the midlatitude storm tracks (Outten et al. (2018)) and in several future  
754 climate integrations performed using the CMIP5 version of the GISS climate model (E2) Rind  
755 et al. (2018). In the latter case, however, the near cessation of the AMOC severely limited, but  
756 did not entirely shut off, poleward heat transport, which was partly maintained through the ocean  
757 subtropical gyre contribution. Our results also show stronger compensation occurring over SH  
758 high latitudes poleward of  $40^\circ\text{S}$ .

759 While the changes in  $T_O$  and  $T_A$  reflect near entire compensation, this compensation is nonethe-  
760 less not perfect and slightly negative, resulting in a net reduction in the total northward combined  
761 atmospheric and oceanic energy transport. This reduction in net poleward energy transport was  
762 also found in Liu et al. (2020), who showed that a weakened AMOC caused a larger energy change  
763 at the Earth's surface than at the TOA (their Figure S.5). In particular, over the NAWH region  
764 they found that more energy was taken from the atmosphere through surface turbulent heat fluxes,  
765 resulting in a situation where the NH atmosphere loses more energy at the surface compared to the  
766 energy that is gained at the TOA (through reduced OLR). In the GISS model we also find that there  
767 is more energy loss at the surface compared to changes at the TOA and that these are primarily  
768 associated with reduced latent heat fluxes (Appendix Figure 4). The reductions in surface latent  
769 heat fluxes occur over the North Atlantic and are strongly shaped by changes in evaporation (not  
770 shown). The exact extent and nature of this compensation, however, is likely shaped strongly by  
771 cloud feedbacks (Zhang et al. (2010)) as discussed more in Section 4b.

## 772 2) MOIST VS. DRY ATMOSPHERIC TRANSPORTS

773 To better understand the nature of the compensation occurring in the GISS model, Figure 12  
774 further decomposes the changes in  $T_A$  into changes in the northward transports of latent heat (Fig.  
775 12a) and dry static energy (Fig. 12b). Over the SH the changes in dry and moist static energy  
776 nearly compensate in all simulations, resulting in weakly negative northward atmospheric transports  
777 poleward of  $\sim 40^\circ\text{S}$  in both the XxCO<sub>2</sub> and SSP 2-4.5 runs. Equatorward of  $\sim 40^\circ\text{S}$ , however, this  
778 behavior transitions in the SSP 2-4.5 C members to net positive northward atmospheric transport  
779 from the SH subtropics towards and across the equator (which compensates the reduction in  
780 oceanic equatorward heat transport in that region evident in Figure 11). This behavior over the SH

## Annual Mean Response in Latent Heat, Dry and Moist Static Energy Transport



788 FIG. 12. Changes in the annual mean atmospheric latent heat (a), dry static energy (b) and total moist static  
 789 energy (c) northward transports, relative to the preindustrial control simulation. Results from the SSP 2-4.5  
 790 ensemble members and the 2-5xCO<sub>2</sub> simulations are shown in the top and bottom panels. The simulations in  
 791 which the AMOC collapses (3xCO<sub>2</sub>, SSP 2-4.5 C) versus recovers (2xCO<sub>2</sub>, SSP 2-4.5 R) are highlighted in the  
 792 red and green lines, respectively.

781 subtropics is distinct from what occurs in the XxCO<sub>2</sub> simulations, in which there is overall reduced  
 782 northward atmospheric transport (and less compensation by the oceanic transports). The fact that  
 783 the oceanic compensation in this region is weaker at 3xCO<sub>2</sub> (relative to the SSP 2-4.5 C members)  
 784 may reflect the differences in simulation length between the abrupt CO<sub>2</sub> and SSP 2-4.5 integrations  
 785 or the fact that at 3xCO<sub>2</sub> there is increased water vapor in the atmosphere in the warmer climate and  
 786 hence increased poleward latent heat transport. Notably, however, the AMOC response in all runs  
 787 has little effect on extratropical latent heat transport over the Southern Hemisphere extratropics.

793 Aside from the subtle differences between the 3xCO<sub>2</sub> and SSP 2-4.5 C runs that occur over the  
 794 SH subtropics, the fact that the changes in dry static energy (DSE) and latent heat transport nearly  
 795 compensate over southern and tropical latitudes in all runs is consistent with the expectation from  
 796 Held and Soden (2006). Interestingly, however, this compensation does not occur over northern  
 797 latitudes spanning ~10°N to ~40°N, resulting in a net increase in poleward moist static energy

798 transport (Fig. 12c). Over these latitudes the increased atmospheric energy transport resulting  
799 from an AMOC collapse is almost entirely due to changes in dry static energy, not latent heat  
800 transport. In particular, DSE transport exhibits a “jump” between  $2\times\text{CO}_2$  and  $3\times\text{CO}_2$  (also evident  
801 in the differences between the SSP 2-4.5 C and SSP 2-4.5 R members) (Fig. 12b); a similar jump is  
802 only evident in the latent heat transports equatorward of  $20^\circ\text{N}$  (which, if anything, enhances energy  
803 transport equatorward, not poleward). The jump in DSE transport over the northern extratropics  
804 saturates for forcings greater than  $3\times\text{CO}_2$ . Further analysis of the evolution of the dry static energy  
805 transports at different latitudes in the northern hemisphere (not shown) reveals that these changes  
806 in DSE transport first emerge between  $30^\circ\text{N}$ - $40^\circ\text{N}$  and propagate thereafter to higher latitudes.

807 The fact that the abrupt increase in atmospheric poleward transport derives primarily from  
808 changes in DSE transport helps in interpreting why a similar shift emerges in the Hadley Cell and  
809 eddy-driven jet, since the Hadley cell fluxes dry static energy poleward (Frierson et al. (2007)).  
810 Indeed, previous energetic definitions of the storm track have appealed directly to DSE (e.g.  
811 latitude of maximum vertically-integrated dry static energy flux (Hoskins and Valdes (1990)).  
812 More recently, Lachmy and Shaw (2018) show that the vertically integrated eddy potential energy  
813 flux shifts in same sense as the vertically integrated eddy DSE flux. They then use the Eliassen-  
814 Palm flux relation to connect these changes in energy fluxes to changes in the eddy momentum  
815 fluxes. Therefore, the fact that these features all shift in concert with each other in our runs should  
816 perhaps not be too surprising.

## 817 **4. Discussion**

### 818 *a. Caveats Concerning Model Biases*

819 One important caveat with our results relates to known biases in vertical mixing in the ocean  
820 component of the GISS model, as discussed in Miller et al. (2021). This biased mixing is  
821 likely related to why E2.1 exhibits a more sensitive AMOC response to a quadrupling of  $\text{CO}_2$ ,  
822 compared to some other CMIP6 models (KB2021). In addition, Rind et al. (2020) showed that the  
823 parameterization of rainfall evaporation associated with moist convective precipitation has a strong  
824 influence on the AMOC sensitivity to greenhouse gas forcing in the E2.1 (and higher top E2.2)  
825 models, likely via its effect on moisture loading in the atmosphere. Thus, in addition to oceanic  
826 processes, atmospheric parameterizations could also be influencing this result.

827 Along with biases in vertical mixing, the ocean component of E2.1 is also low resolution (one  
828 degree). This likely has direct implications for the stability of the AMOC, as discussed in AR2023  
829 (see references therein). In particular, the stability of the AMOC will differ between low resolution  
830 climate models, which exhibit a negative salt-advection feedback (leading to salinification of the  
831 subpolar gyre and AMOC recovery), and eddy-permitting models, which tend to exhibit a stable  
832 AMOC-off state. We emphasize here, however, that throughout we have focused on the response of  
833 the atmospheric circulation given a collapse in the AMOC. Thus, while the particular mechanisms  
834 by which the AMOC is weakened (and subsequently recovers) in E2.1 may be model-specific,  
835 our focus has been on quantifying the atmospheric changes. We also note that Mitevski et al.  
836 (2021) showed that the behavior of the AMOC in E2.1 was similar to the response in CESM-LE;  
837 furthermore that model also featured a nonlinear response in GMST related to a collapse of the  
838 AMOC, albeit one occurring at the transition between  $3xCO_2$  and  $4xCO_2$ .

### 839 *b. Bjerknes Compensation: Cloud Feedbacks and Dry Versus Moist Energy Transports*

840 A key result from our study is that a collapse of the AMOC results in a regime shift in various  
841 components of the NH large-scale circulation and this shift is reflective of an abrupt Bjerknes  
842 compensation that emerges at  $3xCO_2$  and in the SSP 2-4.5 C ensemble members. There are several  
843 aspects of this compensation, however, that require closer examination. Among others, these  
844 include:

#### 845 1) INFLUENCE OF CLOUD FEEDBACKS

846 Mitevski et al. (2022) showed that nonlinearity in ECS occurring between  $2xCO_2$  and  $3xCO_2$   
847 in our model was related to nonlinear variations in the atmospheric feedback parameter and not  
848 to changes in radiative forcing. At the same time, the strength of the Bjerknes compensation in  
849 our model will likely depend on cloud feedbacks, as the right-hand-side of Equation (1) makes  
850 clear (via the  $F_T$  and  $F_S$  terms). For example, Zhang et al. (2010) showed a strong sensitivity  
851 of the tropical climates' response to a freshwater hosing forcing to changes in cloud feedbacks,  
852 showing that in a model with no cloud feedbacks the tropical response to the weakening of the  
853 AMOC (including its southward ITCZ shift) was much smaller. Thus, while the overall Bjerknes  
854 compensation occurring in our model is generally consistent (in its meridional distribution and



855 amplitude) with the results from other similar studies, the exact details of how compensation occurs  
856 is likely to be sensitive to local climate feedbacks which may be model-dependent and/or poorly  
857 constrained by observations. Future work will focus on better understanding how changes in cloud  
858 feedbacks modulate the response of the atmosphere to a weakened AMOC in our model.

## 859 2) ATMOSPHERIC DRY VS. MOIST COMPENSATION

860 One interesting result from this study is that the large compensation in poleward atmospheric  
861 transport that occurs as the AMOC collapses is primarily related to increases in the northward  
862 transport of dry static energy poleward of 20°N (coincident with the edge of the non-monotonically  
863 shifting HC edge) (Fig. 12). This result is initially surprising as it downplays the compensation  
864 that occurs through changes in latent heat transport over northern midlatitudes. Thus, while our  
865 results do show a compensatory latent heat transport occurring in the tropics, this does not occur  
866 over the NH extratropics and is therefore not fundamentally associated with the non-monotonic  
867 behavior in the NH Hadley Cell edge and midlatitude eddy-driven jet.

868 The diminished importance of the latent heat transports over northern midlatitudes is initially  
869 surprising, given that warming in response to increased CO<sub>2</sub> results in an overall increase in  
870 atmospheric water vapor. Upon further reflection, however, this effect of enhanced global warming  
871 needs to be considered in the context of both the reduced Arctic warming and poleward shifted  
872 EKE evident in Figure 4. The former can, via cooling, reduce the total moisture available for  
873 northward transport, while the latter would impact the efficiency with which subtropical moisture  
874 is transported poleward to higher latitudes. In our results it appears that these changes compensate,  
875 resulting in no net AMOC imprint on the latent heat transports over northern extratropical latitudes  
876 (Fig. 10a, bottom). While disentangling these contributions is beyond the scope of this study, we  
877 do comment on the consistent results shown in Figure S5 of Mitevski et al. (2021), who identified  
878 a much stronger non-monotonicity present in the edge of the dry zone (P-E) compared to NH  
879 specific humidity. While this suggests that the circulation changes are themselves responsible for  
880 the behavior of the latent heat transports (and not vice versa), more work is needed to understand  
881 the underlying mechanism present in our model and whether this behavior is also exhibited in other  
882 models (or the real atmosphere).

## 883 5. Conclusions

884 Here we have documented the atmospheric response to a CO<sub>2</sub>-induced AMOC collapse using  
885 the CMIP6 version of the NASA GISS climate model (E2.1). Using simulations from an  
886 identically forced (SSP 2-4.5) ensemble in which the AMOC collapses and recovers in two and  
887 eight members, respectively, we have isolated the atmospheric response to a spontaneous collapse  
888 of the AMOC in the context of a warming climate, absent any external perturbations that may  
889 interfere with the model’s internal dynamics. By comparison, previous studies have all needed  
890 to employ (negative) freshwater flux perturbations or similar AMOC “locking” methods (Liu  
891 et al. (2020), Orihuela-Pinto et al. (2022)). We then placed the atmospheric response in the  
892 SSP 2-4.5 simulations in the broader context of a set of integrations in which CO<sub>2</sub> is abruptly  
893 increased, run both using fully coupled atmosphere-ocean (FOM) and slab-ocean (SOM) config-  
894 urations, in which changes in ocean heat flux convergences are respectively included and neglected.

895

896 Our main results are as follows:

897

- 898 • In our model a sustained decline and eventual collapse of the AMOC results in a strengthening  
899 of the NH Hadley cell and the northern midlatitude jet, as well as an abrupt northward shift  
900 of the Hadley Cell edge in the lower troposphere. Quite remarkably, these features dominate  
901 the large-scale atmospheric circulation response that occurs in the NH moving from 2xCO<sub>2</sub>  
902 to 3xCO<sub>2</sub>.
- 903 • For certain variables (i.e., HC strength, EKE) an ultimate collapse of the AMOC produces  
904 changes that are *opposite* in sign to the response to increased CO<sub>2</sub> forcing occurring in the  
905 absence of ocean circulation changes.
- 906 • The regime shift in the NH large-scale circulation reflects an abrupt Bjerknes compensation  
907 that emerges in the 3xCO<sub>2</sub> and collapsed SSP 2-4.5 C simulations. This compensation is  
908 located further south (~40°N) of what is often considered to be the main region of maximum  
909 ocean-atmosphere compensation (70°N) (Shaffrey and Sutton (2006)) and reflects a key role  
910 for the midlatitude storm tracks in the coupled system’s response to a warmer climate.

911 • The impact of the AMOC on the large-scale NH circulation occurs mainly through its influence  
912 on mean free-tropospheric temperature gradients, not GMST. This finding reinforces growing  
913 evidence that the climate’s “dynamical sensitivity” does not scale with equilibrium climate  
914 sensitivity (Grise and Polvani (2016), Ceppi et al. (2018)), particularly in the presence of a  
915 collapsed AMOC .

916 The regime shift in NH dynamics resulting from an AMOC collapse in our model is, to the best  
917 of our knowledge, the first time that such behavior has been documented for a CMIP class model.  
918 While previous studies have also reported nonlinear behaviors in Hadley Cell strength (Levine and  
919 Schneider (2011), O’Reilly et al. (2016)) these studies have employed mainly idealized models. In  
920 addition to the changes in the Hadley Cell we also identify a regime shift in the behavior of the  
921 northern storm tracks. This result brings to mind the findings from Caballero and Langen (2005),  
922 who showed that poleward energy transport increases over a range of increasing surface temperature  
923 but saturates in the low-gradient, high temperature regime. As in our study, they attribute this  
924 “low-gradient” paradox to increasing tropospheric static stability and the poleward migration of  
925 the storm tracks. However, they too employed a highly idealized (aquaplanet) model and find that  
926 this saturation in storm track behavior is related to a saturation of latent heat transport. Our results,  
927 by comparison, highlight the role of compensatory dry static energy transports and suggests  
928 that studies accounting for dynamic ocean-atmospheric coupling (i.e., changes in vertical and  
929 horizontal ocean heat fluxes) may come to different conclusions about the nature of compensation  
930 in the atmosphere.

931 In addition to contributing to improved understanding of the coupled atmosphere-ocean response  
932 to a weakening of the AMOC, our results also have a practical implication for the purpose of  
933 developing storylines of atmospheric circulation changes (Zappa and Shepherd (2017)) and for  
934 interpreting model differences in projected storm tracks. In particular, while the use of “global  
935 warming levels” applied throughout the IPCC AR6 report may suffice for understanding the global  
936 hydrological cycle (Hausfather et al. (2022)) here we have shown that this does not hold true for  
937 projections of the NH jet stream and Hadley Cell edge. This underscores the need to understand  
938 the direct impact of the AMOC on meridional temperature gradients and not only on surface  
939 temperature.

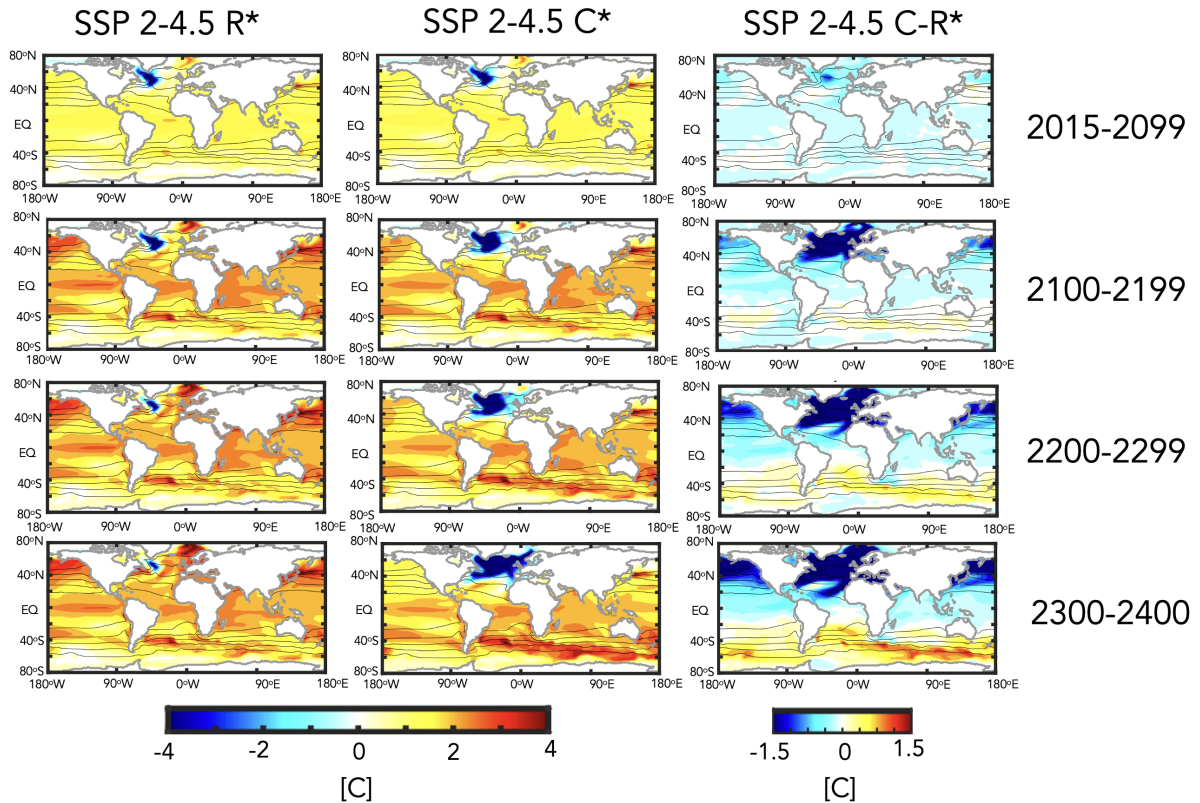
940 Finally, preliminary analysis of the high-top GISS climate model (E2.2 (Rind et al. (2020), Orbe  
941 et al. (2020)) suggests a different sensitivity of the AMOC compared to E2.1 (occurring between  
942  $3xCO_2$  and  $4xCO_2$ ). Understanding these differences and how they are reflected in different  
943 Bjerknæs compensations will be described in a follow-up paper.

944 *Acknowledgments.* C.O. thanks Ivan Mitevski for processing the zonally varying eddy kinetic  
945 energy fields that were used as part of this analysis. Climate modeling at GISS is supported  
946 by the NASA Modeling, Analysis and Prediction program, and resources supporting this work  
947 were provided by the NASA High-End Computing (HEC) Program through the NASA Center for  
948 Climate Simulation (NCCS) at Goddard Space Flight Center.

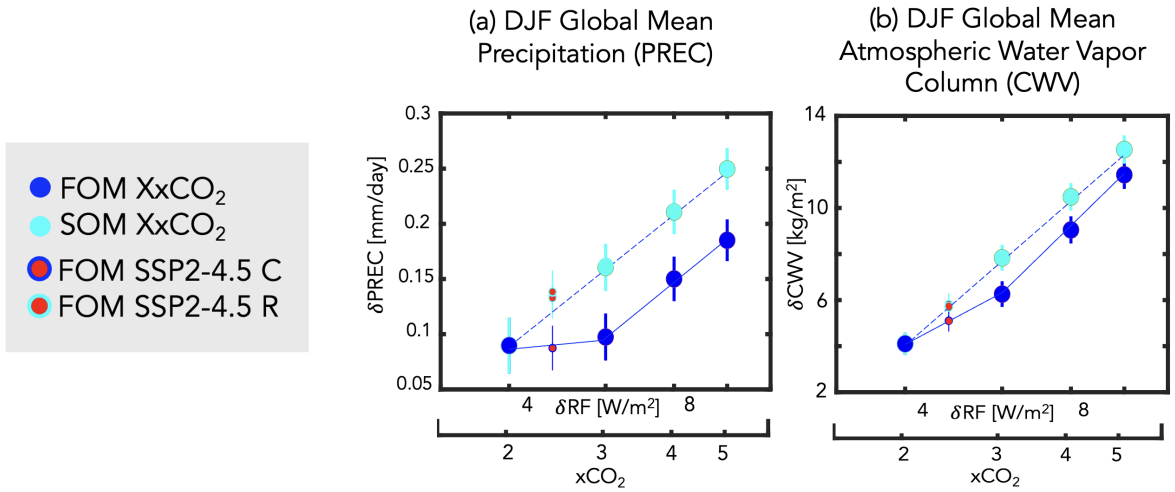
949 *Data availability statement.* The CMIP6 SSP 2-4.5 data used in this study is available from  
950 the Earth System Grid Federation (ESGF) (<https://esgf-node.llnl.gov/search/cmip6/>)  
951 or from the NASA Center for Climate Simulations (NCCS) (<https://portal.nccs.nasa.gov/datashare/giss/cmip6/>). The specific simulations used here are a subset of the historical  
952 r[1-10]i1p1f2 (doi:87010.22033/ESGF/CMIP6.7127) and SSP 2-4.5 r[1-10]i1p1f2 (doi:10.  
953 22033/ESGF/CMIP6.7415) runs. The XxCO<sub>2</sub> data used to produce the figures in the study is  
954 publicly available in a Zenodo repository at <https://doi.org/10.5281/zenodo.3901624>.  
955 The authors acknowledge the World Climate Research Programme's Working Group on Coupled  
956 Modeling and we thank all climate modeling groups for making available their model output.  
957 All GISS ModelE components are open source and available at [https://www.giss.nasa.gov/  
958 tools/modelE/](https://www.giss.nasa.gov/tools/modelE/).  
959

**Appendix Figures**

## Evolution of DJF Response in Sea Surface Temperature ( $\delta$ SST)

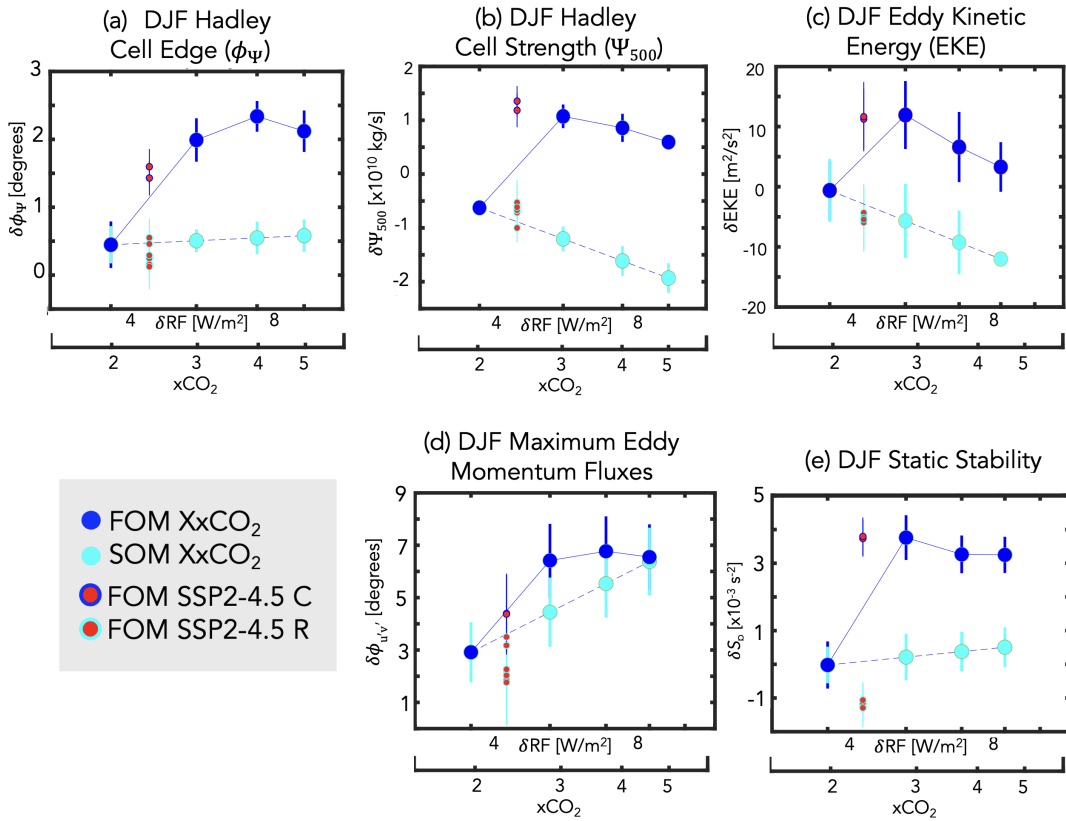


962 FIG. A1. The evolution of the DJF sea surface temperature difference, relative to the preindustrial control  
 963 simulation, in one of the SSP 2-4.5 recovered (R) (left) and collapsed (C) ensemble members (middle). The  
 964 difference between the SSP 2-4.5 recovered and collapsed ensemble members is also shown (right). Note that  
 965 only one ensemble member is used due to the different recovery times of the AMOC among the “recovered”  
 966 ensemble members prior to year 2400. Climatological mean values from the preindustrial control simulation are  
 967 denoted in the black contours.

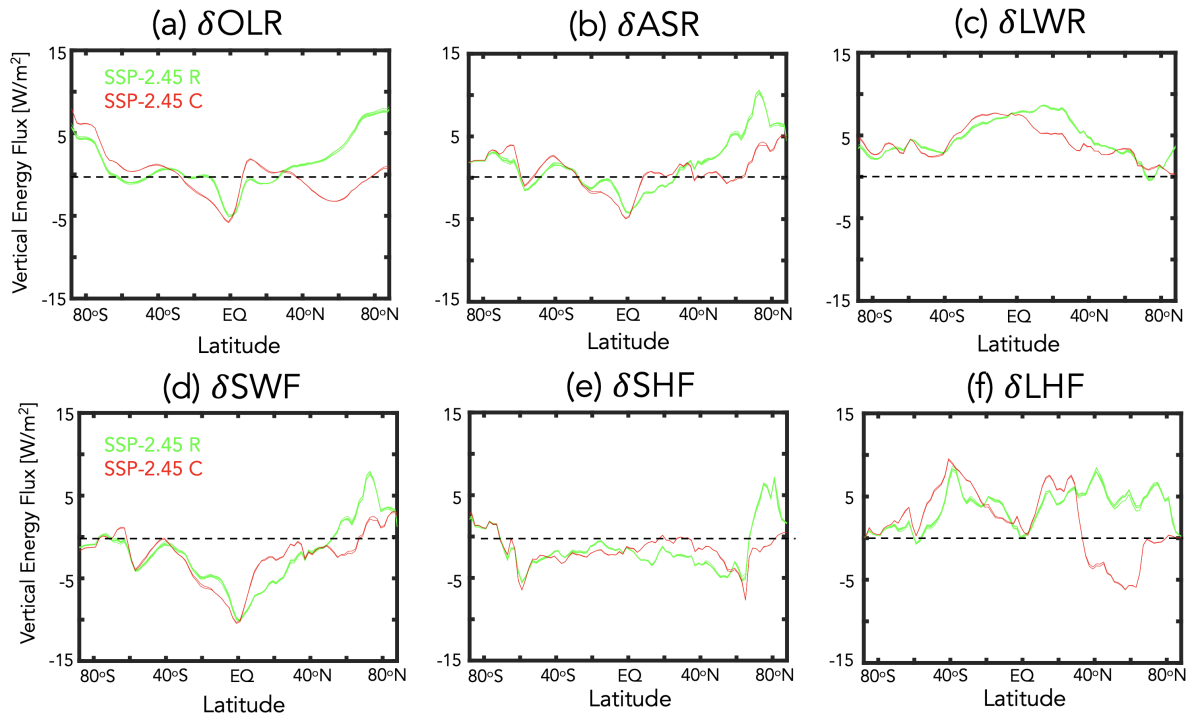


968 FIG. A2. Changes in DJF global mean precipitation (a) and atmospheric column water vapor (b), plotted as a  
 969 function of the associated radiative forcing (RF), calculated from the expression  $5.35 \ln(NxCO_2/1xCO_2)$  (Byrne  
 970 and Goldblatt (2014)) where, for each run, N is the  $CO_2$  multiple of the PI value (2.4, for the case of the SSP  
 971 2-4.5 ensemble members). Results from the abrupt 2-5 $xCO_2$  fully coupled atmosphere-ocean model (FOM) and  
 972 slab ocean model (SOM) results are shown in the blue and cyan filled circles. The FOM SSP 2-4.5 recovered and  
 973 collapsed ensemble members are also shown in the red circles (cyan and blue outlines, respectively). Interannual  
 974 variability for each metric is indicated by the vertical bars.





975 FIG. A3. Changes in various DJF Northern Hemisphere (NH) dynamical metrics, plotted as a function of  
 976 associated radiative forcing. Specifically, shown are the Hadley Cell edge ( $\phi_{UAS}$ ) (a), Hadley Cell strength ( $\Psi_{500}$ )  
 977 (b), NH column eddy kinetic energy (EKE) (c), latitude of the maximum NH eddy momentum fluxes (d) and NH  
 978 midlatitude dry static stability (e). The quantities in (a), (b) and (d) are defined in Section 2, while the zonally  
 979 averaged EKE and static stability changes have both been averaged over 300-1000 hPa and 30°N-60°N. Results  
 980 from the abrupt 2-5 $xCO_2$  fully coupled atmosphere-ocean model (FOM) and slab ocean model (SOM) results  
 981 are shown in the blue and cyan filled circles. The FOM SSP 2-4.5 recovered and collapsed ensemble members  
 982 are shown in the red circles (cyan and blue outlines, respectively). Interannual variability for each metric is  
 983 indicated by the vertical bars.



984 FIG. A4. Changes in the annual mean top of the atmosphere outgoing longwave radiation (OLR) (a) and  
 985 absorbed shortwave radiation (ASR) (b) and the downward fluxes of radiation at the surface, decomposed into  
 986 longwave (LWF) (c) and shortwave (SWF) (d) components. The fluxes of latent and sensible heat at the surface  
 987 (LHF and SHF) are shown in (e) and (f), respectively. All changes are shown for the SSP 2-4.5 collapsed (C)  
 988 (red) and SSP 2-4.5 recovered (R) (green) ensemble members and are defined relative to the preindustrial control  
 989 simulation.

## 990 **References**

- 991 Adam, O., and Coauthors, 2018: The TropD software package (v1): standardized methods for  
992 calculating tropical-width diagnostics. *Geoscientific Model Development*, **11 (10)**, 4339–4357.
- 993 Bellomo, K., M. Angeloni, S. Corti, and J. von Hardenberg, 2021: Future climate change shaped  
994 by inter-model differences in Atlantic meridional overturning circulation response. *Nature Com-*  
995 *munications*, **12 (1)**, 1–10.
- 996 Bjerknes, J., 1964: Atlantic air-sea interaction. *Advances in geophysics*, Vol. 10, Elsevier, 1–82.
- 997 Brayshaw, D. J., T. Woollings, and M. Vellinga, 2009: Tropical and extratropical responses of  
998 the North Atlantic atmospheric circulation to a sustained weakening of the MOC. *Journal of*  
999 *Climate*, **22 (11)**, 3146–3155.
- 1000 Byrne, B., and C. Goldblatt, 2014: Radiative forcing at high concentrations of well-mixed green-  
1001 house gases. *Geophysical Research Letters*, **41 (1)**, 152–160.
- 1002 Caballero, R., and P. L. Langen, 2005: The dynamic range of poleward energy transport in an  
1003 atmospheric general circulation model. *Geophysical Research Letters*, **32 (2)**.
- 1004 Caesar, L., S. Rahmstorf, A. Robinson, G. Feulner, and V. Saba, 2018: Observed fingerprint of a  
1005 weakening Atlantic ocean overturning circulation. *Nature*, **556 (7700)**, 191–196.
- 1006 Ceppi, P., G. Zappa, T. G. Shepherd, and J. M. Gregory, 2018: Fast and slow components of  
1007 the extratropical atmospheric circulation response to CO<sub>2</sub> forcing. *Journal of Climate*, **31 (3)**,  
1008 1091–1105.
- 1009 Chemke, R., and L. M. Polvani, 2019: Exploiting the abrupt 4× CO<sub>2</sub> scenario to elucidate tropical  
1010 expansion mechanisms. *Journal of Climate*, **32 (3)**, 859–875.
- 1011 Chemke, R., L. Zanna, C. Orbe, L. T. Sentman, and L. M. Polvani, 2022: The future intensification  
1012 of the North Atlantic winter storm track: the key role of dynamic ocean coupling. *Journal of*  
1013 *Climate*, **35 (8)**, 2407–2421.
- 1014 Cheng, W., J. C. Chiang, and D. Zhang, 2013: Atlantic meridional overturning circulation (AMOC)  
1015 in CMIP5 models: RCP and historical simulations. *Journal of Climate*, **26 (18)**, 7187–7197.

- 1016 Cronin, T. W., and M. F. Jansen, 2016: Analytic radiative-advective equilibrium as a model for  
1017 high-latitude climate. *Geophysical Research Letters*, **43** (1), 449–457.
- 1018 Deser, C., and A. S. Phillips, 2009: Atmospheric circulation trends, 1950–2000: The relative roles  
1019 of sea surface temperature forcing and direct atmospheric radiative forcing. *Journal of Climate*,  
1020 **22** (2), 396–413.
- 1021 Drijfhout, S., G. J. Van Oldenborgh, and A. Cimadoribus, 2012: Is a decline of AMOC causing the  
1022 warming hole above the North Atlantic in observed and modeled warming patterns? *Journal of*  
1023 *Climate*, **25** (24), 8373–8379.
- 1024 Frierson, D. M., I. M. Held, and P. Zurita-Gotor, 2007: A gray-radiation aquaplanet moist GCM.  
1025 Part II: Energy transports in altered climates. *Journal of the Atmospheric Sciences*, **64** (5),  
1026 1680–1693.
- 1027 Gervais, M., J. Shaman, and Y. Kushnir, 2019: Impacts of the North Atlantic warming hole in  
1028 future climate projections: Mean atmospheric circulation and the North Atlantic jet. *Journal of*  
1029 *Climate*, **32** (10), 2673–2689.
- 1030 Grise, K. M., and L. M. Polvani, 2014: The response of midlatitude jets to increased co2:  
1031 Distinguishing the roles of sea surface temperature and direct radiative forcing. *Geophysical*  
1032 *Research Letters*, **41** (19), 6863–6871.
- 1033 Grise, K. M., and L. M. Polvani, 2016: Is climate sensitivity related to dynamical sensitivity?  
1034 *Journal of Geophysical Research: Atmospheres*, **121** (10), 5159–5176.
- 1035 Grise, K. M., and L. M. Polvani, 2017: Understanding the time scales of the tropospheric circulation  
1036 response to abrupt co2 forcing in the southern hemisphere: Seasonality and the role of the  
1037 stratosphere. *Journal of Climate*, **30** (21), 8497–8515.
- 1038 Haarsma, R., F. Selten, and S. Drijfhout, 2015: Decelerating Atlantic meridional overturning  
1039 circulation main cause of future west european summer circulation changes. *Environmental*  
1040 *Research Letters*, **10** (9).
- 1041 Hausfather, Z., K. Marvel, G. A. Schmidt, J. W. Nielsen-Gammon, and M. Zelinka, 2022: Climate  
1042 simulations: Recognize the ‘hot model’ problem. Nature Publishing Group.

- 1043 Held, I. M., 1993: Large-scale dynamics and global warming. *Bulletin of the American Meteorological Society*, **74** (2), 228–242.
- 1044
- 1045 Held, I. M., and B. J. Soden, 2006: Robust responses of the hydrological cycle to global warming. *Journal of climate*, **19** (21), 5686–5699.
- 1046
- 1047 Hoskins, B. J., and P. J. Valdes, 1990: On the existence of storm-tracks. *Journal of Atmospheric Sciences*, **47** (15), 1854–1864.
- 1048
- 1049 Jackson, L., R. Kahana, T. Graham, M. Ringer, T. Woollings, J. Mecking, and R. Wood, 2015: Global and european climate impacts of a slowdown of the AMOC in a high resolution GCM. *Climate Dynamics*, **45** (11), 3299–3316.
- 1050
- 1051
- 1052 James, R., R. Washington, C.-F. Schleussner, J. Rogelj, and D. Conway, 2017: Characterizing half-a-degree difference: a review of methods for identifying regional climate responses to global warming targets. *Wiley Interdisciplinary Reviews: Climate Change*, **8** (2), e457.
- 1053
- 1054
- 1055 Josey, S. A., J. J.-M. Hirschi, B. Sinha, A. Ducez, J. P. Grist, and R. Marsh, 2018: The recent Atlantic cold anomaly: Causes, consequences, and related phenomena. *Annual Review of Marine Science*, **10**, 475–501.
- 1056
- 1057
- 1058 Kelley, M., and Coauthors, 2020: GISS-E2. 1: Configurations and climatology. *Journal of Advances in Modeling Earth Systems*, **12** (8), e2019MS002025.
- 1059
- 1060 Lachmy, O., and T. Shaw, 2018: Connecting the energy and momentum flux response to climate change using the Eliassen-Palm relation. *Journal of Climate*, **31** (18), 7401–7416.
- 1061
- 1062 Lau, N.-C., H. Tennekes, and J. M. Wallace, 1978: Maintenance of the momentum flux by transient eddies in the upper troposphere. *Journal of Atmospheric Sciences*, **35** (1), 139–147.
- 1063
- 1064 Levine, X. J., and T. Schneider, 2011: Response of the Hadley circulation to climate change in an aquaplanet GCM coupled to a simple representation of ocean heat transport. *Journal of the Atmospheric Sciences*, **68** (4), 769–783.
- 1065
- 1066
- 1067 Lim, G. H., and J. M. Wallace, 1991: Structure and evolution of baroclinic waves as inferred from regression analysis. *Journal of Atmospheric Sciences*, **48** (15), 1718–1732.
- 1068

- 1069 Liu, W., A. V. Fedorov, S.-P. Xie, and S. Hu, 2020: Climate impacts of a weakened Atlantic  
1070 Meridional Overturning Circulation in a warming climate. *Science Advances*, **6** (26), eaaz4876.
- 1071 Lu, J., G. A. Vecchi, and T. Reichler, 2007: Expansion of the Hadley cell under global warming.  
1072 *Geophysical Research Letters*, **34** (6).
- 1073 Magnusdottir, G., and R. Saravanan, 1999: The response of atmospheric heat transport to zonally-  
1074 averaged SST trends. *Tellus A: Dynamic Meteorology and Oceanography*, **51** (5), 815–832.
- 1075 Marshall, J., J. R. Scott, K. C. Armour, J.-M. Campin, M. Kelley, and A. Romanou, 2015: The  
1076 ocean’s role in the transient response of climate to abrupt greenhouse gas forcing. *Climate*  
1077 *Dynamics*, **44** (7), 2287–2299.
- 1078 Meinshausen, M., and Coauthors, 2020: The shared socio-economic pathway (SSP) greenhouse  
1079 gas concentrations and their extensions to 2500. *Geoscientific Model Development*, **13** (8),  
1080 3571–3605.
- 1081 Menary, M. B., and R. A. Wood, 2018: An anatomy of the projected North Atlantic warming hole  
1082 in CMIP5 models. *Climate Dynamics*, **50** (7), 3063–3080.
- 1083 Menzel, M. E., D. Waugh, and K. Grise, 2019: Disconnect between Hadley cell and subtropical jet  
1084 variability and response to increased CO<sub>2</sub>. *Geophysical Research Letters*, **46** (12), 7045–7053.
- 1085 Miller, R. L., and Coauthors, 2021: CMIP6 historical simulations (1850–2014) with GISS-E2. 1.  
1086 *Journal of Advances in Modeling Earth Systems*, **13** (1), e2019MS002034.
- 1087 Mitevski, I., C. Orbe, R. Chemke, L. Nazarenko, and L. M. Polvani, 2021: Non-monotonic  
1088 response of the climate system to abrupt CO<sub>2</sub> forcing. *Geophysical Research Letters*, **48** (6),  
1089 e2020GL090861.
- 1090 Mitevski, I., L. M. Polvani, and C. Orbe, 2022: Asymmetric warming/cooling response to CO<sub>2</sub>  
1091 increase/decrease mainly due to non-logarithmic forcing, not feedbacks. *Geophysical Research*  
1092 *Letters*, **49** (5), e2021GL097133.
- 1093 Nazarenko, L. S., and Coauthors, 2022: Future climate change under SSP emission scenarios with  
1094 GISS-E2. 1. *Journal of Advances in Modeling Earth Systems*, e2021MS002871.

- 1095 Orbe, C., and Coauthors, 2020: GISS model E2. 2: A climate model optimized for the middle  
1096 atmosphere—2. Validation of large-scale transport and evaluation of climate response. *Journal*  
1097 *of Geophysical Research: Atmospheres*, **125** (24), e2020JD033 151.
- 1098 O'Reilly, C. H., M. Huber, T. Woollings, and L. Zanna, 2016: The signature of low-frequency  
1099 oceanic forcing in the Atlantic Multidecadal Oscillation. *Geophysical Research Letters*, **43** (6),  
1100 2810–2818.
- 1101 Orihuela-Pinto, B., M. H. England, and A. S. Taschetto, 2022: Interbasin and interhemispheric  
1102 impacts of a collapsed Atlantic Overturning Circulation. *Nature Climate Change*, 1–8.
- 1103 Outten, S., I. Esau, and O. H. Otterå, 2018: Bjerknes compensation in the CMIP5 climate models.  
1104 *Journal of Climate*, **31** (21), 8745–8760.
- 1105 Pedro, J. B., M. Jochum, C. Buizert, F. He, S. Barker, and S. O. Rasmussen, 2018: Beyond  
1106 the bipolar seesaw: Toward a process understanding of interhemispheric coupling. *Quaternary*  
1107 *Science Reviews*, **192**, 27–46.
- 1108 Rahmstorf, S., J. E. Box, G. Feulner, M. E. Mann, A. Robinson, S. Rutherford, and E. J. Schaffer-  
1109 night, 2015: Exceptional twentieth-century slowdown in Atlantic Ocean overturning circulation.  
1110 *Nature climate change*, **5** (5), 475–480.
- 1111 Riahi, K., and Coauthors, 2011: RCP 8.5—A scenario of comparatively high greenhouse gas  
1112 emissions. *Climatic Change*, **109**, 33–57.
- 1113 Rind, D., G. A. Schmidt, J. Jonas, R. Miller, L. Nazarenko, M. Kelley, and J. Romanski, 2018:  
1114 Multicentury instability of the Atlantic meridional circulation in rapid warming simulations with  
1115 GISS ModelE2. *Journal of Geophysical Research: Atmospheres*, **123** (12), 6331–6355.
- 1116 Rind, D., and Coauthors, 2020: GISS Model E2. 2: A climate model optimized for the mid-  
1117 dle atmosphere—Model structure, climatology, variability, and climate sensitivity. *Journal of*  
1118 *Geophysical Research: Atmospheres*, **125** (10), e2019JD032 204.
- 1119 Robson, J., P. Ortega, and R. Sutton, 2016: A reversal of climatic trends in the North Atlantic since  
1120 2005. *Nature Geoscience*, **9** (7), 513–517.

- 1121 Romanou, A., and Coauthors, Under Review: Stochastic bifurcation of the North Atlantic cir-  
1122 culation under a mid-range future climate scenario with the NASA-GISS ModelE. *Journal of*  
1123 *Climate*.
- 1124 Samset, B., and Coauthors, 2016: Fast and slow precipitation responses to individual climate  
1125 forcings: A PDRMIP multimodel study. *Geophysical Research Letters*, **43** (6), 2782–2791.
- 1126 Santer, B. D., T. M. Wigley, M. E. Schlesinger, and J. F. Mitchell, 1990: Developing climate  
1127 scenarios from equilibrium GCM results.
- 1128 Schmidt, D. F., and K. M. Grise, 2017: The response of local precipitation and sea level pressure  
1129 to Hadley cell expansion. *Geophysical Research Letters*, **44** (20), 10–573.
- 1130 Schneider, T., 2006: The general circulation of the atmosphere. *Annu. Rev. Earth Planet. Sci.*, **34**,  
1131 655–688.
- 1132 Shaffrey, L., and R. Sutton, 2006: Bjerknes compensation and the decadal variability of the energy  
1133 transports in a coupled climate model. *Journal of Climate*, **19** (7), 1167–1181.
- 1134 Shaw, T., and A. Voigt, 2015: Tug of war on summertime circulation between radiative forcing  
1135 and sea surface warming. *Nature Geoscience*, **8** (7), 560–566.
- 1136 Shepherd, T. G., 2014: Atmospheric circulation as a source of uncertainty in climate change  
1137 projections. *Nature Geoscience*, **7** (10), 703–708.
- 1138 Smith, D. M., R. Eade, N. J. Dunstone, D. Fereday, J. M. Murphy, H. Pohlmann, and A. A. Scaife,  
1139 2010: Skilful multi-year predictions of Atlantic hurricane frequency. *Nature Geoscience*, **3** (12),  
1140 846–849.
- 1141 Tebaldi, C., and J. M. Arblaster, 2014: Pattern scaling: Its strengths and limitations, and an update  
1142 on the latest model simulations. *Climatic Change*, **122** (3), 459–471.
- 1143 Thompson, D. W., and T. Birner, 2012: On the linkages between the tropospheric isentropic  
1144 slope and eddy fluxes of heat during Northern Hemisphere winter. *Journal of the Atmospheric*  
1145 *Sciences*, **69** (6), 1811–1823.
- 1146 Timmermann, A., and Coauthors, 2007: The influence of a weakening of the Atlantic meridional  
1147 overturning circulation on ENSO. *Journal of Climate*, **20** (19), 4899–4919.



- 1148 Vallis, G. K., P. Zurita-Gotor, C. Cairns, and J. Kidston, 2015: Response of the large-scale structure  
1149 of the atmosphere to global warming. *Quarterly Journal of the Royal Meteorological Society*,  
1150 **141 (690)**, 1479–1501.
- 1151 Vellinga, M., and R. A. Wood, 2008: Impacts of thermohaline circulation shutdown in the twenty-  
1152 first century. *Climatic Change*, **91 (1)**, 43–63.
- 1153 Vial, J., C. Cassou, F. Codron, S. Bony, and Y. Ruprich-Robert, 2018: Influence of the Atlantic  
1154 meridional overturning circulation on the tropical climate response to CO<sub>2</sub> forcing. *Geophysical  
1155 Research Letters*, **45 (16)**, 8519–8528.
- 1156 Waugh, D. W., and Coauthors, 2018: Revisiting the relationship among metrics of tropical expan-  
1157 sion. *Journal of Climate*, **31 (18)**, 7565–7581.
- 1158 Weijer, W., W. Cheng, O. A. Garuba, A. Hu, and B. Nadiga, 2020: CMIP6 models predict  
1159 significant 21<sup>st</sup> century decline of the Atlantic meridional overturning circulation. *Geophysical  
1160 Research Letters*, **47 (12)**, e2019GL086075.
- 1161 Woollings, T., J. M. Gregory, J. G. Pinto, M. Reyers, and D. J. Brayshaw, 2012: Response of  
1162 the North Atlantic storm track to climate change shaped by ocean–atmosphere coupling. *Nature  
1163 Geoscience*, **5 (5)**, 313–317.
- 1164 Wu, L., C. Li, C. Yang, and S.-P. Xie, 2008: Global teleconnections in response to a shutdown of  
1165 the Atlantic meridional overturning circulation. *Journal of Climate*, **21 (12)**, 3002–3019.
- 1166 Zappa, G., and T. G. Shepherd, 2017: Storylines of atmospheric circulation change for European  
1167 regional climate impact assessment. *Journal of Climate*, **30 (16)**, 6561–6577.
- 1168 Zhang, R., and T. L. Delworth, 2005: Simulated tropical response to a substantial weakening of  
1169 the Atlantic thermohaline circulation. *Journal of Climate*, **18 (12)**, 1853–1860.
- 1170 Zhang, R., and T. L. Delworth, 2006: Impact of Atlantic multidecadal oscillations on India/Sahel  
1171 rainfall and Atlantic hurricanes. *Geophysical Research Letters*, **33 (17)**.
- 1172 Zhang, R., S. M. Kang, and I. M. Held, 2010: Sensitivity of climate change induced by the  
1173 weakening of the Atlantic meridional overturning circulation to cloud feedback. *Journal of  
1174 Climate*, **23 (2)**, 378–389.